Article

Current Biology

A Role for Astroglial Calcium in Mammalian Sleep and Sleep Regulation

Graphical Abstract

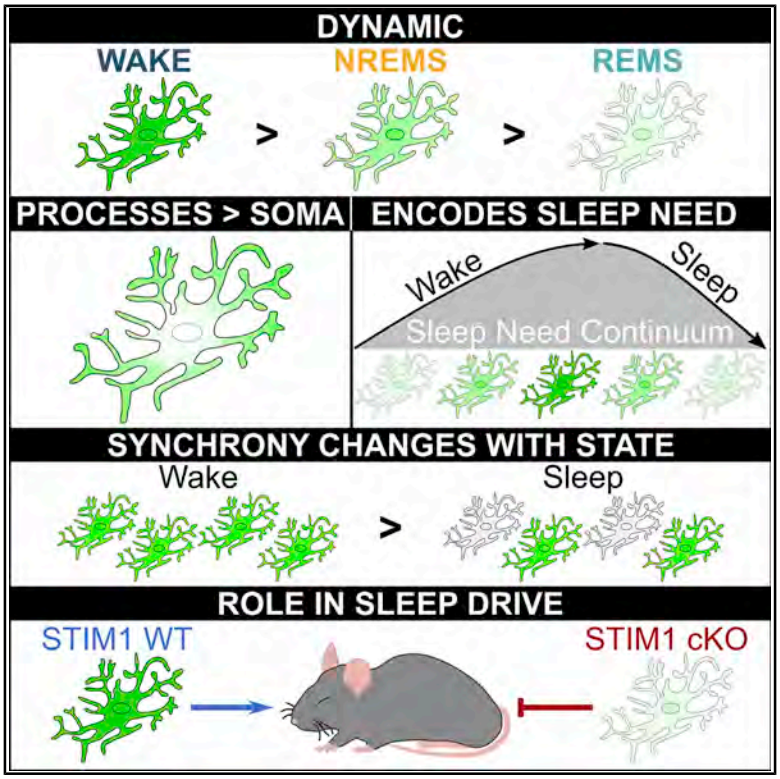

Highlights

- Astroglial Ca^{2+} signals change dynamically with sleep, wake, and sleep loss
- Astroglial Ca^{2+} encodes changes in sleep need
- Synchrony of astroglial Ca^{2+} signals changes with vigilance state and sleep need
- Reduced astroglial Ca^{2+} via knockout of STIM1 reduces sleep drive after sleep loss

Authors

Ashley M. Ingiosi, Christopher R. Hayworth, Daniel O. Harvey, Kristan G. Singletary, Michael J. Rempe, Jonathan P. Wisor, Marcos G. Frank

Correspondence

marcos.frank@wsu.edu

In Brief

Ingiosi et al. describe how astroglial Ca^{2+} signals change dynamically across sleep and wake and after sleep loss using *in vivo* imaging methods. Synchrony of astroglial Ca^{2+} signals decreases during sleep compared to wake and after sleep deprivation. STIM1 regulation of astroglial Ca^{2+} plays a role in the normal compensatory response to sleep loss.

Ingiosi et al., 2020, Current Biology *30*, 4373–4383
November 16, 2020
https://doi.org/10.1016/j.cub.2020.08.052

CellPress

Current Biology

CellPress

Article

A Role for Astroglial Calcium in Mammalian Sleep and Sleep Regulation

Ashley M. Ingiosi,[1] Christopher R. Hayworth,[1] Daniel O. Harvey,[1] Kristan G. Singletary,[1] Michael J. Rempe,[1,2] Jonathan P. Wisor,[1] and Marcos G. Frank[1,3,*]

[1]Department of Biomedical Sciences, Elson S. Floyd College of Medicine, Washington State University, East Spokane Falls Boulevard, Spokane, WA 99202, USA

[2]Department of Mathematics and Computer Science, Whitworth University, West Hawthorne Road, Spokane, WA 99251, USA

[3]Lead Contact

*Correspondence: marcos.frank@wsu.edu

https://doi.org/10.1016/j.cub.2020.08.052

SUMMARY

Mammalian sleep expression and regulation have historically been thought to reflect the activity of neurons. Changes in other brain cells (glia) across the sleep-wake cycle and their role in sleep regulation are comparatively unexplored. We show that sleep and wakefulness are accompanied by state-dependent changes in astroglial activity. Using a miniature microscope in freely behaving mice and a two-photon microscope in head-fixed, unanesthetized mice, we show that astroglial calcium signals are highest in wake and lowest in sleep and are most pronounced in astroglial processes. We also find that astroglial calcium signals during non-rapid eye movement sleep change in proportion to sleep need. In contrast to neurons, astrocytes become less synchronized during non-rapid eye movement sleep after sleep deprivation at the network and single-cell level. Finally, we show that conditionally reducing intracellular calcium in astrocytes impairs the homeostatic response to sleep deprivation. Thus, astroglial calcium activity changes dynamically across vigilance states, is proportional to sleep need, and is a component of the sleep homeostat.

INTRODUCTION

The glial cells known as astrocytes are hypothesized to play important roles in mammalian sleep [1]. They secrete sleep-inducing substances, and sleep influences the morphology, gene expression, and proliferation of different glial cells [1]. Astrocytes are also densely concentrated throughout the brain including regions important for sleep and wake [2]. They surround synapses, respond non-linearly to neurotransmitters, and via several different mechanisms (e.g., metabolism, neurotransmitter uptake, and gliotransmission) modulate neuronal activity [3–6]. This confers upon these cells the ability to integrate and respond to changes in neurons, providing a feedback mechanism to regulate neuronal activity [3–5, 7, 8]. There are, however, two critical and unaddressed issues regarding the role of astrocytes in sleep.

A key feature of mammalian sleep is that it is accompanied by widespread and diverse changes in cortical neuronal activity [9]. In the late 1950s, this observation led to a revolution in our understanding of sleep. Sleep was originally described as a "passive" state in which the sleeping brain was quiescent [10]. However, the discovery of rapid eye movement sleep (REMS) demonstrated that sleep is accompanied by dynamic changes in neuronal activity [10–12]. Sleep has been subsequently discussed and described almost entirely based on neuronal measurements. Astrocytes, however, could be just as dynamic as neurons across the sleep-wake cycle, albeit in different ways. If true, this could trigger a fundamental change in our understanding of sleep by revealing an entirely different level of brain organization that also changes with sleep. This intriguing possibility has not been investigated. Previous sleep studies of astrocytes relied on *ex vivo* measurements (e.g., changes in mRNAs or proteins) [13–15] or did not measure natural patterns of activity in sleep [16].

Homeostasis is a second key feature of sleep. In all mammals, sleep intensity (as measured by electroencephalographic [EEG] activity) and/or sleep duration increases as a function of prior time spent awake [17]. Sleep homeostasis has also been historically thought to be primarily a product of neurons [1]. Recent findings suggest that astrocytes may be part of the mammalian sleep homeostat [2, 18], but the cellular mechanisms governing this putative feedback circuit are controversial and largely unexplored [1]. It is also unknown whether essential astroglial signaling pathways, notably intracellular calcium (Ca^{2+}), encode sleep need or are essential components of sleep homeostasis. Unlike neurons, astrocytes show minimal electrical activity and use Ca^{2+} to mediate intracellular functions [19]. We performed several experiments to investigate these two issues.

RESULTS

Astroglial Ca^{2+} Signals Change with Vigilance State

We first determined whether astroglial intracellular Ca^{2+} signals change across naturally cycling vigilance states. To do this, we expressed the genetically encoded Ca^{2+} indicator GCaMP6f selectively in frontal cortex astrocytes of C57BL/6J mice (n = 6; Figure 1A). This is because the frontal cortex shows the greatest dynamic range of non-rapid eye movement sleep (NREMS) slow wave activity (SWA), a canonical index of mammalian sleep

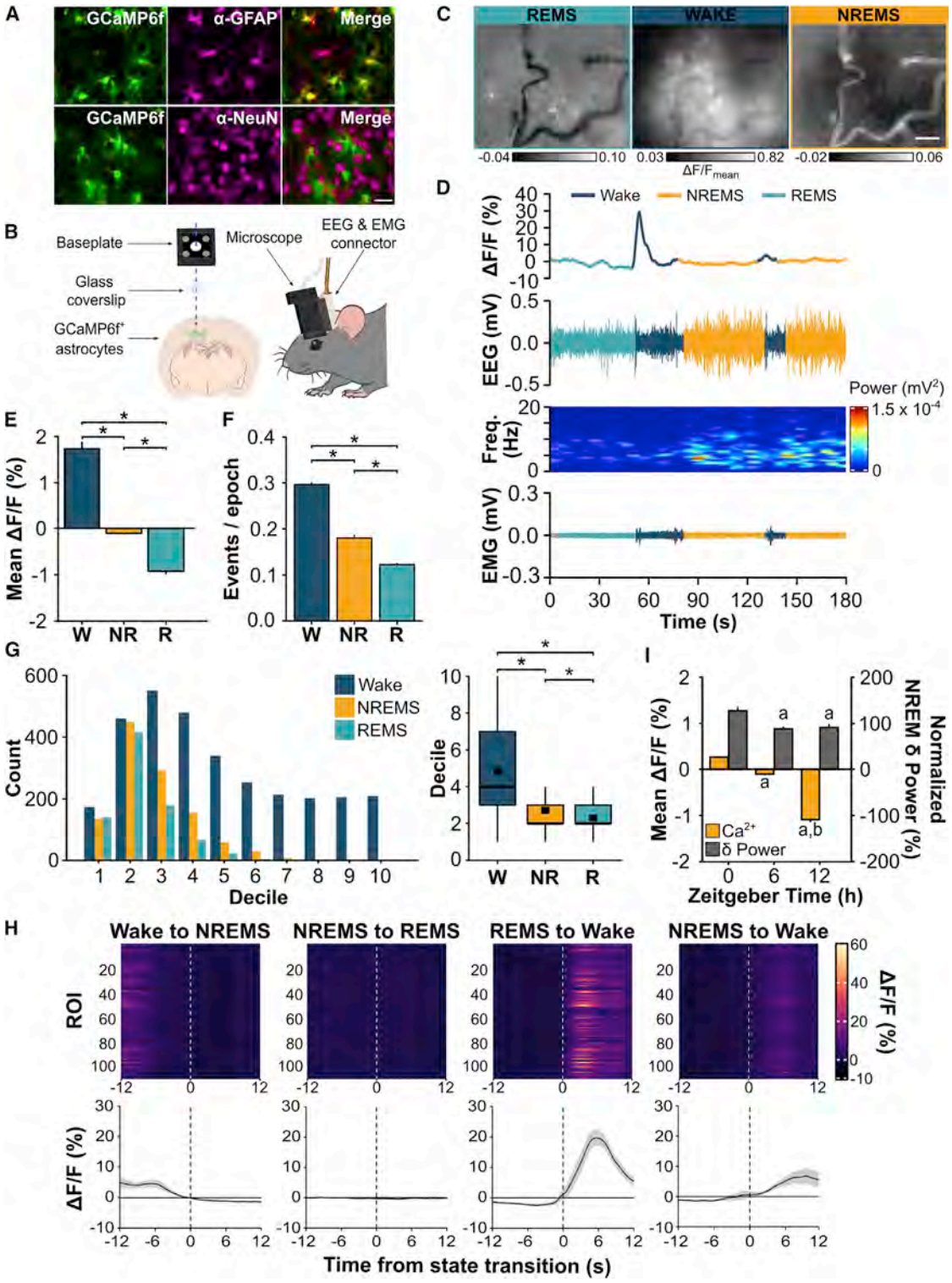

Figure 1. Astroglial Ca^{2+} Signals Change with Vigilance State and Time of Day

(A) Representative images from one mouse showing microinjection of AAV2/5 *GfaABC$_1$D*-GCaMP6f in cortex results in selective expression of GCaMP6f in GFAP$^+$ astrocytes (top) but not in NeuN$^+$ neurons (bottom). GCaMP6f labeling (green) is native, whereas astrocytes (GFAP; magenta) and neurons (NeuN; magenta) are immunolabeled. 40× objective; scale bar, 20 μm.

(B) Cartoon showing dual EEG & EMG recording and astroglial Ca^{2+} imaging in the frontal cortex through a cranial window.

(C) Maximum projection ΔF/F images of Ca^{2+} imaging in astrocytes during wake, NREMS, and REMS from Video S1 using the miniature microscope and Inscopix Data Processing Software. The time incorporated for each image corresponds to the traces shown in (D) (REMS: 50 s; wake: 28 s; NREMS: 48 s). Scale bar, 100 μm.

(legend continued on next page)

need [2, 20]. We then recorded EEG and electromyographic (EMG) activity while simultaneously imaging changes in astroglial GCaMP6f Ca^{2+} signals in unanesthetized, freely behaving mice using a head-mounted, epifluorescent miniature microscope (Figures 1B–1D; Figure S1; Video S1).

We found significant between-state differences in astroglial Ca^{2+} signals based on three metrics: mean GCaMP6f fluorescence (ΔF/F), frequency of GCaMP6f Ca^{2+} events, and amplitude of GCaMP6f Ca^{2+} events (see STAR Methods for details). All three measures showed state-dependent changes (Figure 1E, mean ΔF/F: $\chi^2 = 914.39$, $p < 0.001$; Figure 1F, frequency of Ca^{2+} events: $\chi^2 = 295.64$, $p < 0.001$; Figure 1G, amplitude of Ca^{2+} events: $\chi^2 = 779.48$, $p < 0.001$). Mean ΔF/F, frequency of Ca^{2+} events and amplitude of Ca^{2+} events were all greatest in wake and lowest in REMS. The negative mean ΔF/F values in Figure 1E indicate that, on average, fluorescent values for sleep were less than the median fluorescent value used to calculate ΔF/F (see STAR Methods for details). In other words, negative ΔF/F values do not signify that absolute Ca^{2+} concentrations were less than 0. Instead, this means that cytosolic Ca^{2+} of astrocytes was lower in sleep compared to wake. An additional striking observation was the transition from REMS to wake, which was accompanied by large changes in ΔF/F (Figure 1H; Video S1). Collectively, these data show that astrocytes (like neurons) display dynamic changes in activity across the sleep-wake cycle.

We next explored whether astroglial Ca^{2+} signals change across the rest phase. This would provide insight into whether astrocytes encode sleep need because sleep need (as measured by NREM SWA) is high at the beginning of the rest phase (Zeitgeber time [ZT] 0) and discharged by the end (ZT12) [21, 22]. We found that mean ΔF/F during NREMS was maximal at ZT0 and reached a nadir at ZT12 ($F(2, 1566.18) = 85.93$, $p < 0.001$) in parallel with changes in NREM SWA (Figure 1I; $F(2, 387.07) = 9.13$, $p < 0.001$). Changes in wake and REMS, however, were more variable over time (Figures S1C and S1D) as were changes in frequency of Ca^{2+} events and amplitude of Ca^{2+} events (data not shown). These results suggest that astrocytes change their activity in parallel with sleep need, and this is most consistently found in NREMS.

Astroglial Ca^{2+} Signals Are More Dynamic in the Processes Compared to Somata

We then determined whether changes in Ca^{2+} signals were uniform throughout the astrocyte or compartmentalized in the soma versus the processes. This was of interest because Ca^{2+} signals in astroglial processes can occur independently from the soma and may reflect different types of functions [19, 23–27]. Because the signal captured by the miniature microscope includes both somatic and process activity, we used two-photon microscopy to more precisely examine how astroglial Ca^{2+} signals change in these subcellular regions in frontal cortex of unanesthetized C57BL/6J mice (n = 4) across vigilance states (Figures 2A and 2B; Video S2). During wake, NREMS, and REMS, astroglial processes showed greater frequency of single Ca^{2+} events compared to somata (Figure 2C; wake: $U = 41221.00$, $p < 0.001$; NREMS: $U = 456161.50$, $p < 0.001$; REMS: $U = 45023.00$, $p < 0.001$). Furthermore, mean ΔF/F was greater in astroglial processes compared to somata during wake (Figure 2D; $U = 99967.50$, $p < 0.001$) and NREMS ($U = 87228.00$, $p < 0.001$). REMS exhibited a similar trend ($U = 63555.00$, $p = 0.102$). Further analyses measuring ΔF/F differences between somata and processes revealed that the bias toward processes was largest in wake and REMS (Figure 2E; $\chi^2 = 267.57$, $p < 0.001$). Overall, these findings indicate that astroglial activity is not uniform within the cell during sleep and wake but biased to processes.

We next determined how the spread and movement of astroglial Ca^{2+} signals within the processes of single astrocytes changes with vigilance state. Within individual astrocytes, Ca^{2+} signals display diverse spatiotemporal patterns, which may serve different neurobiological functions [19, 27]. Using an event-based analysis program, Astrocyte Quantitative Analysis (AQuA) [28], Ca^{2+} events within single astrocytes were identified via a series of previously established parameters [28] (see STAR Methods) using two-photon microscopy data from unanesthetized adult mice. We restricted our measurements to previously used metrics that capture the heterogeneity of Ca^{2+} events within astroglial processes [28]. Astroglial Ca^{2+} events were divided into "propagating" (Figures 3A and 3B) and "static" events as described previously (Figures 3C and 3D) [28]. Briefly, the AQuA algorithm defines propagating events as Ca^{2+} events that grow or move toward or away from the soma (Figure 3A), whereas static events are Ca^{2+} events that do not propagate (Figure 3C) [28]. These events were further parsed into subcellular events that started closest to the soma (<50%) and events that started farthest from the soma (>50%) based on the distance between the soma and the cell border (Figure S2A) [28]. We next determined the area (i.e., size in μm^2) and duration (i.e., length of event onset to event offset in seconds) of individual astroglial Ca^{2+} events. We focused on wake and NREMS at ZT6. Similar analyses were not performed in REMS as there were too few REMS episodes of sufficient length for AQuA processing. Under baseline conditions, the area and duration of propagating (Figure 3B) and static (Figure 3D) Ca^{2+} events were generally greater during wake compared to NREMS (see Table S1 for statistics). The area and duration of Ca^{2+} events also tended to be larger in regions farther from the soma (i.e., >50%), which was

(D) Representative Ca^{2+}-induced fluorescent trace from one ROI from Video S1, EEG, EEG power spectrogram, and EMG in each vigilance state.
(E) Mean (±SEM) ΔF/F during wake (W), NREMS (NR), and REMS (R) at ZT6 (Friedman test).
(F) Number of astroglial Ca^{2+} events per 4 s vigilance state epoch expressed as means ± SEM at ZT6 (Friedman test).
(G) Distribution of Ca^{2+} event amplitudes organized by smallest (low deciles) to largest (high deciles) values during wake, NREMS, and REMS and boxplot comparisons at ZT6. Black squares in boxplots denote means (wake = 4.84; NREMS = 2.71; REMS = 2.30; Friedman test).
(H) Heatmaps show Ca^{2+}-induced fluorescence traces from 110 regions of interest (ROI) from a representative mouse during the 12 s before and after transitions between vigilance states. Line plots are mean ΔF/F (±SEM) during state transitions under baseline conditions for n = 6 mice. Vertical, dashed lines indicate time of state transition.
(I) Mean ΔF/F during NREMS and baseline NREMS EEG delta (δ) power (i.e., NREM SWA; 0.5–4 Hz) at ZT0, 6, and 12. NREM δ power is expressed as a percentage of the last 4 h of the light period. Values are means ± SEM. [a], different from ZT0; [b], different from ZT6 (linear mixed-effects model). Group means are from n = 586 individual ROIs from 6 mice. *Vigilance state differences. $p < 0.05$. See also Figure S1 and Video S1.

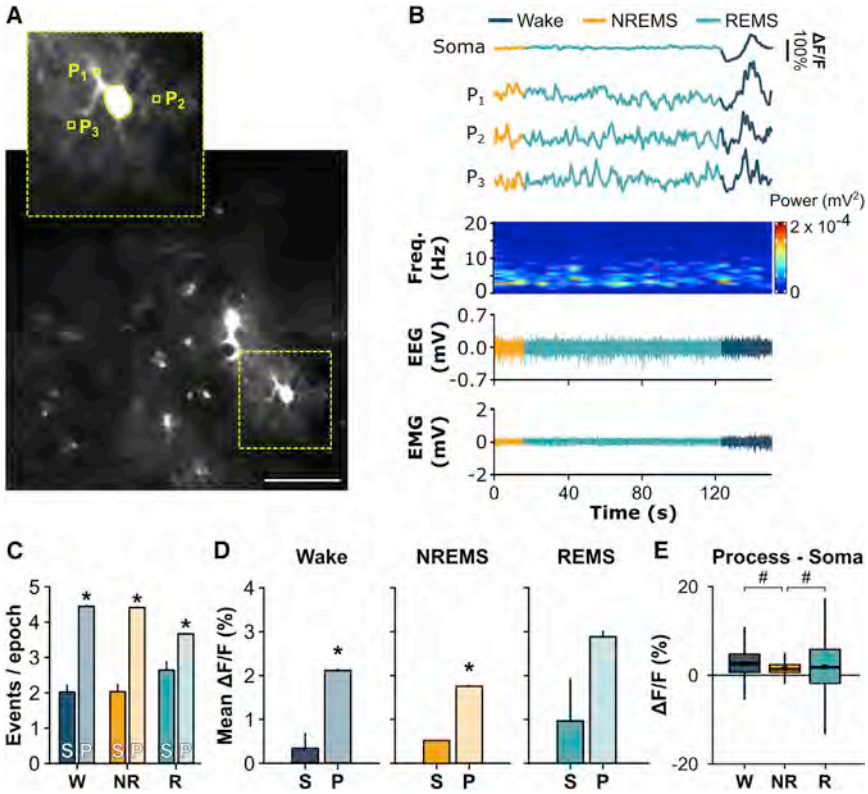

Figure 2. Astroglial Ca^{2+} Signals Differ between Somata and Processes

(A) Sum t stack projection image of GCaMP6f^{+} astrocytes from two-photon microscopy. Inset shows examples of regions of interest for the soma and processes (P_1–P_3) for a single astrocyte depicted in (B). Scale bar, 10 μm.

(B) Representative Ca^{2+} traces from an astrocyte soma and 3 of its respective processes (P_1–P_3) with aligned EEG power spectrogram, EEG, and EMG.

(C) Number of Ca^{2+} events per 4 s vigilance state epoch in somata (S) and processes (P) expressed as means ± SEM under baseline conditions for wake (W), NREMS (NR), and REMS (R) during the rest phase (Mann-Whitney U test).

(D) Mean (±SEM) ΔF/F for wake, NREMS, and REMS for astroglial somata (S) and processes (P) under baseline conditions during the rest phase (Mann-Whitney U test).

(E) Difference scores for ΔF/F between process ROIs and their respective soma for W, NR, and R during the rest phase (Friedman test). Black squares in boxplots denote means (W = 2.40%; NR = 1.40%; R = 2.31%). Group means are from n = 60 somata and n = 6,074 process ROIs (i.e., individual squares within the grid) from 4 mice. *Different from somata. #Difference between vigilance states. $p < 0.05$. See also Video S2.

most evident for propagating events (Figure 3B; Table S1). We also performed a more comprehensive analysis in which we plotted the area and duration of all events against the starting proximity to the soma (i.e., not based on the 50% delineation). In confirmation of our initial results, the area of propagating Ca^{2+} events increased as they moved away from the soma (Figure S2). Additionally, the duration of static Ca^{2+} signals was longer in events starting closer to the soma (Figure S2). These findings show that the spread and movement of astroglial Ca^{2+} events changes from wake to sleep and reveal a subcellular heterogeneity of Ca^{2+} signals in natural brain states.

Changes in Astroglial Ca^{2+} Encode Sleep Need

We next directly tested whether changes in astroglial Ca^{2+} encode changes in sleep need. This was suggested by our time-of-day measures (Figure 1I), but sleep homeostasis is traditionally explored using sleep deprivation (SD). More specifically, in these experiments we determined whether astroglial Ca^{2+} signals increased with SD and decreased during recovery sleep. To do this, we sleep deprived freely behaving mice for 6 h (ZT0–6; a procedure that produces maximal sleep pressure in mice [29]) and imaged astroglial Ca^{2+} using two-photon microscopy (Figure 4A) and the miniature microscope (Figure S3) during the recovery period. We report those Ca^{2+} metrics that significantly varied from baseline values.

Two-photon microscopy showed that SD increased mean ΔF/F depending on vigilance state and subcellular location. We found that, averaged across all states, mean ΔF/F increased immediately after SD at ZT6 (when sleep need is maximally discharging [21, 22]) and then declined in parallel with changes in NREM SWA at ZT12 (ZT6, 187.55% ± 20.56% versus baseline; ZT12, 106.00% ± 10.51% versus baseline). These ΔF/F changes were greater in the processes versus astroglial somata (Figure 4B; processes: $\chi^2 = 106.28$, $p < 0.001$). We then examined within-state changes. Wake was accompanied by a trend toward lower somatic mean ΔF/F (Figure 4C; Figure S3), which contributed to a shift in Ca^{2+} toward the processes (Figure 4D; $Z = -29.37$, $p < 0.001$) at ZT6 compared to baseline. This shift was maintained at ZT12 (Figure S3B) and accompanied by reduced mean ΔF/F in the somata and processes compared to baseline levels at ZT12 (Figure S3A). During NREMS, mean ΔF/F in the processes was elevated after SD at ZT6 relative to baseline (Figure 4E; $Z = -16.05$, $p < 0.001$; Figure 4F; $Z = -6.53$, $p < 0.001$) and reached baseline levels at ZT12 (Figure S3A). Ca^{2+} signals during REMS were more variable (Figure S3), but there was not a sufficient amount of REMS at ZT6 for analyses. Similar results were obtained using the miniature microscope (Figures S3C and S3D). Overall, these results indicated that SD-induced changes in astroglial Ca^{2+} were most consistently found during NREMS and primarily reflected increases in the processes.

To further determine changes in astrocyte Ca^{2+} driven by sleep need, we applied AQuA analyses, as described above in the baseline period. At ZT6, SD increased the area and decreased the duration of propagating (Figure 3B) and static (Figure 3D) events in wake and NREMS (Table S1). In processes farthest from the soma (i.e., >50%), the duration of propagating events lengthened during NREMS (Figure 3B; Table S1). Using the same analysis described above, we also found a positive

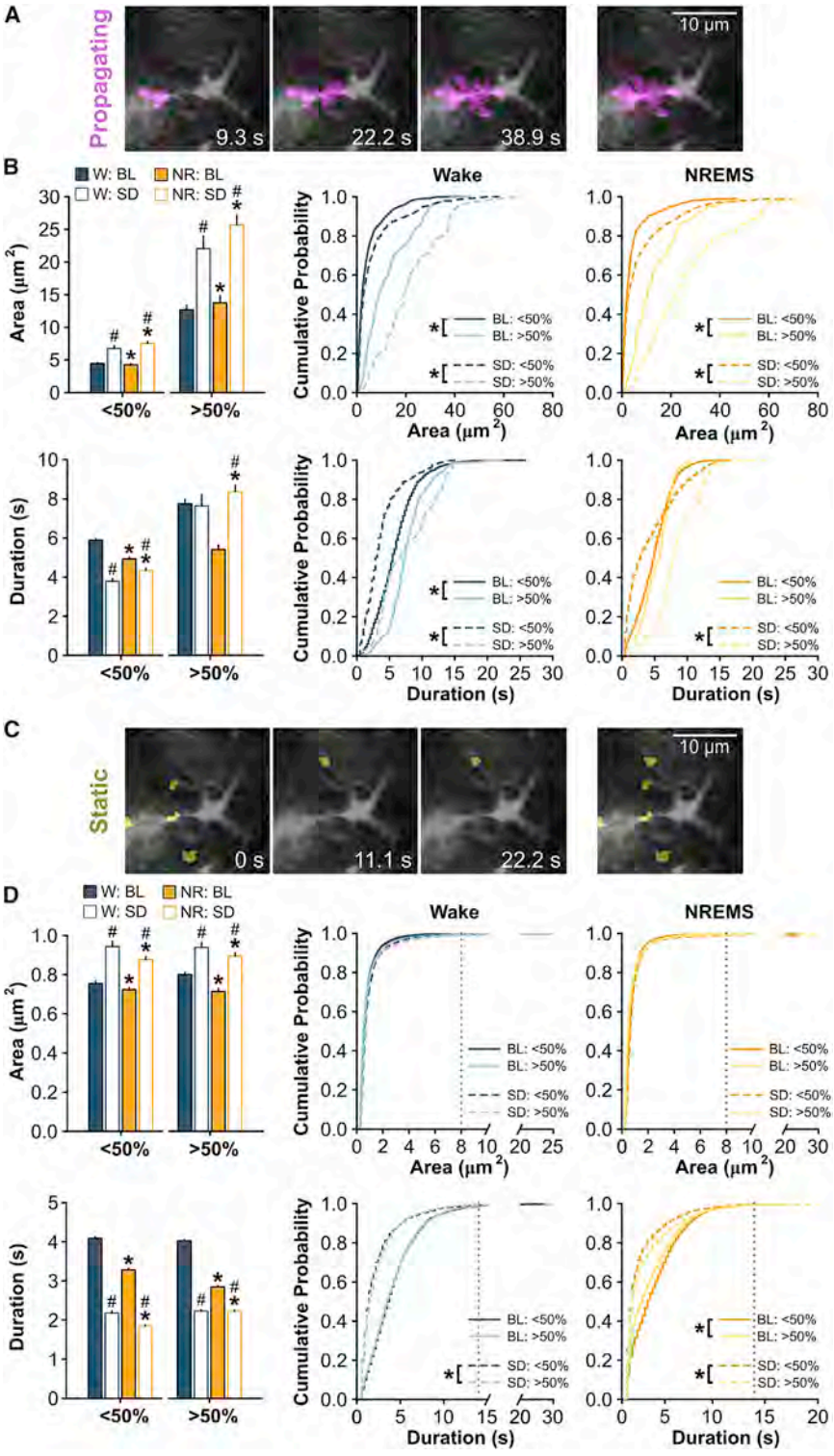

Figure 3. The Spread and Movement of Ca^{2+} Events within Astroglial Processes Changes across Vigilance States

(A) Representative images of a propagating astroglial Ca^{2+} event over time imaged with two-photon microscopy and identified via AQuA (irrespective of state).

(B) Average event area (top) and duration (bottom) for propagating events in the processes during wake (W) and NREMS (NR) under baseline (BL) and sleep-deprived (SD) conditions at ZT6. Events are shown for those events starting in subcellular regions closest to the soma (<50%) and farthest from the soma (>50%). Segregation of regions is based on the halfway point between the soma and the cell border. Values are expressed as means ± SEM (left; W versus NR: Wilcoxon signed-rank test; BL versus SD: Mann-Whitney U test) and cumulative probabilities (middle, right; Kolmogorov-Smirnov test).

(C) Representative images of five static astroglial Ca^{2+} events over time imaged with two-photon microscopy and identified via AQuA (irrespective of state).

(D) Average event area (top) and duration (bottom) for static events in the processes during W and NR under BL and SD conditions at ZT6. Dashed, vertical gray lines on the cumulative probability plots indicate a saturation point defined by a cumulative probability $\geq$0.99. Statistical comparisons were made between values to the left of this line. Values are expressed as means ± SEM (left; W versus NR: Wilcoxon signed-rank test; BL versus SD: Mann-Whitney U test) and cumulative probabilities (middle, right; Kolmogorov-Smirnov). Group means are from n = 27 cells for BL and n = 28 cells for SD from 4 mice. *Different from W for bar plots or different from >50% for cumulative probability plots. #Different from BL. $p < 0.05$.

See also Figure S2 and Tables S1 and S2.

correlation between the area and duration of propagating Ca^{2+} events during NREMS based on initial proximity to the soma after SD (Figure S2C). Similar relationships were observed in the duration of static events during NREMS (Figure S2D). These findings demonstrate that Ca^{2+} spatiotemporal signals are altered by SD within single astrocytes.

Synchrony of Astroglial Ca^{2+} Signals Changes with Vigilance State and Sleep Need

Sleep is accompanied by changes in the synchrony of neuronal networks [9]. It was therefore of interest to explore patterns of synchronous activity across astroglial networks during different vigilance states. Although astrocytes *in vitro* show highly synchronous activity [30], their behavior across natural brain states is unknown. Using the miniature microscope (Figures 5A–5C), we found that astrocytes were highly synchronized in all states, but this synchrony was greatest during wake and lowest in sleep (Figure 5B; $\chi^2 = 544.73$, $p < 0.001$). As SD increases synchronized neuronal activity in NREMS [31], we then determined whether 6 h SD changed the network synchrony of cortical astrocytes. Interestingly, SD reduced synchronous activity in NREMS but increased it in REMS at ZT6 (Figure 5B;

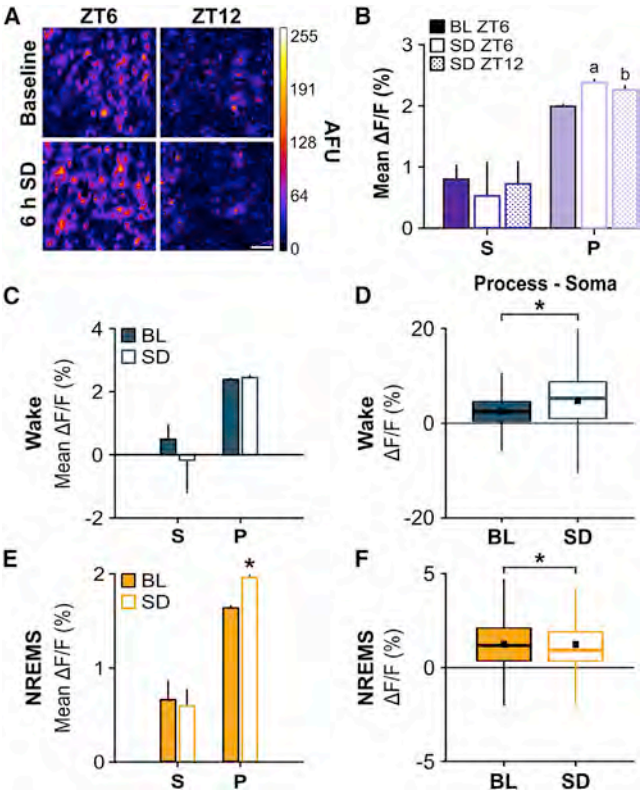

Figure 4. Sleep Deprivation Alters Astroglial Ca^{2+} Signals

(A) Maximum projection images of GCaMP6f^{+} astrocytes at ZT6 (left) & ZT12 (right) for baseline (top; BL) and 6 h sleep deprivation (bottom; SD) conditions from two-photon microscopy. Scale bar, 10 μm. Color bar shows arbitrary fluorescence units (AFUs).

(B) Mean ΔF/F values from all vigilance states for somata (S) and processes (P) during BL ZT6, SD ZT6, and SD ZT12. [a]Difference from BL ZT6 processes; [b]difference from SD ZT6 processes (Friedman test).

(C and E) Mean ΔF/F values during (C) wake and (E) NREMS at ZT6 under BL and SD conditions (Wilcoxon signed-rank test).

(D and F) Distributions of differences in ΔF/F values between processes and their soma at ZT6 under BL and SD conditions for (D) wake and (F) NREMS (Wilcoxon signed-rank test). Black squares in boxplots denote means (wake: BL = 2.20%, SD = 4.35%; NREMS: BL = 1.21%, SD = 1.24%).

Values are means ± SEM for (B), (C), and (E). Group means are from n = 60 somata and n = 6,074 process ROIs from 4 mice. *Different from BL. $p < 0.05$. See also Figure S3.

$\chi^2 = 45.44$, $p < 0.001$). These results are in contrast to the electrical activity of cortical neurons which becomes more synchronous during NREMS following SD [31].

We then used two-photon microscopy and AQuA analyses to perform similar measurements within single astrocytes at ZT6 to determine whether similar changes occurred at the level of single astrocytes. We used separate AQuA algorithms for this purpose that measured the number of Ca^{2+} events that either overlapped in time (temporally co-occurring events; Figure 5D) or in space (spatially co-occurring events; Figure 5E) [28]. Temporally and spatially co-occurring events were determined within individual astrocytes and included all events within the cell irrespective of the event's location (e.g., soma, processes; see STAR Methods) [28]. After SD, the number of temporally co-occurring events (e.g., synchrony) decreased during wake and NREMS (Figure 5D; wake: U = 13439267.00, $p < 0.001$; NREMS: U = 56505290.50, $p < 0.001$). Similarly, the number of spatially co-occurring events decreased during wake and NREMS after SD (Figure 5E; wake: U = 20418397.00, $p < 0.001$; NREMS: U = 72492813.50, $p < 0.001$). Analyses were not performed in REMS as there were too few REMS episodes of sufficient length for AQuA processing. Collectively, these data show that astroglial Ca^{2+} signals, at the network and single-cell level, became less synchronous during the recovery from SD.

Stromal Interaction Molecule 1 Regulation of Astroglial Intracellular Ca^{2+} Is Important for Sleep Homeostasis

The time-of-day and SD experiments strongly suggested that astroglial Ca^{2+} encodes sleep need. To more directly determine whether astroglial Ca^{2+} was required for sleep homeostasis, we inducibly deleted STIM1 in astrocytes by crossing STIM1$^{fl/fl}$ mice with GFAP-Cre/ERT2$^{Tg+/-}$ mice. STIM1-mediated store-operated Ca^{2+} entry (SOCE) is an essential mechanism by which the intracellular Ca^{2+} concentration is elevated [32]. Inhibiting STIM1 impairs SOCE in astrocytes [32], indicating that STIM1 is an integral component of astroglial Ca^{2+} regulation. We first determined that Cre recombination occurred selectively in astrocytes using a floxed LacZ Cre reporter line (R26R$^{fl/fl}$) crossed with GFAP-Cre/ERT2$^{Tg+/-}$ mice (Figure S4). We next verified that astroglial Ca^{2+} was lower in freely behaving mice lacking STIM1 in astrocytes (GSTIM1 conditional knockout [cKO]) compared to GSTIM1 wild-type (WT) mice using two approaches. In one approach, GSTIM1 WT (n = 3) and cKO (n = 4) mice were injected with methoxamine (20 mg/kg intraperitoneally) [33], an α1-adrenergic receptor agonist (Figure S4). Methoxamine is a potent driver of Ca^{2+} activity in cortical astrocytes [34]. We found that the GSTIM1 cKO astroglial Ca^{2+} response to methoxamine was reduced compared to GSTIM1 WT mice (Figure S4). For the other approach using a different group of mice, we determined that astroglial Ca^{2+} was lower in GSTIM1 cKO mice (n = 4) under baseline and SD conditions compared to GSTIM1 WT mice (n = 3; Figure 6A; BL: U = 12236.00, $p < 0.001$; SD: U = 11866.00, $p < 0.001$; see also Figure S5). Next, we tested whether reduced astroglial Ca^{2+} affected sleep and wake behavior under baseline conditions and after 6 h SD in freely behaving mice. Interestingly, GSTIM1 WT (n = 8) and cKO (n = 9) mice were largely similar for time spent in each vigilance state, bout frequency, bout duration, and EEG spectral power under baseline conditions (Figures S5A–S5D). Diurnal/nocturnal patterns of running wheel activity, cage activity, and core body temperature also did not differ between GSTIM1 WT (n = 3) and cKO (n = 3) mice (Figure S6). After SD, however, the normal homeostatic response to SD was blunted in GSTIM1 cKO mice as measured by NREM SWA (0.5–4.0 Hz; Figure 6B; genotype × time effect: $F(2, 26) = 4.00$, $p = 0.031$ and Figures S5F–S5H), NREM SWA in the lower frequency bands (0.0–1.5 Hz; Figure 6C; genotype effect: $F(1, 13) = 7.00$, $p = 0.020$), and sleep time (Figure 6D, $t(15) = 2.23$, $p = 0.041$ and Figure 6E, genotype effect for wake: $F(1, 15) = 4.98$, $p = 0.041$). These findings demonstrate that astroglial STIM1-mediated Ca^{2+} contributes to sleep homeostasis.

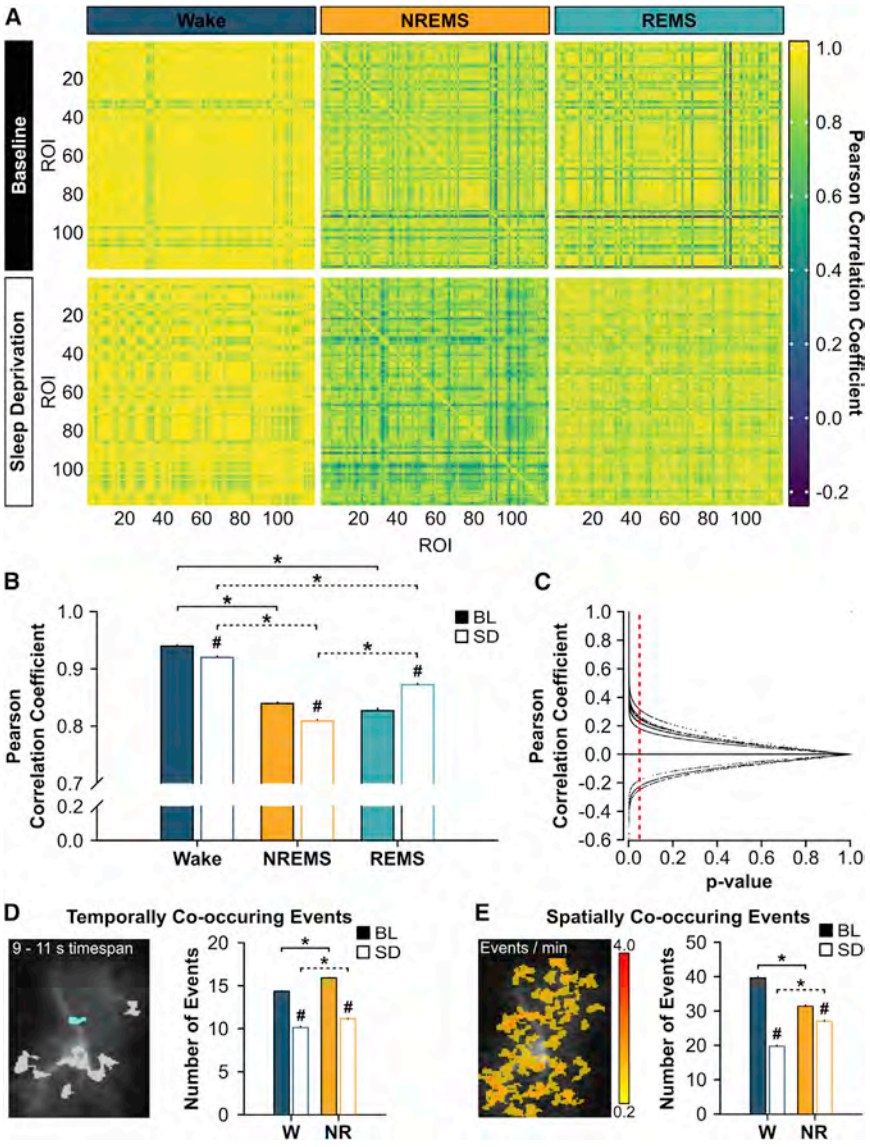

Figure 5. Synchrony of Astroglial Ca^{2+} Signals Changes across Sleep and Wake and after Sleep Deprivation

(A) Pearson correlation coefficient matrices of ΔF/F values across many astrocytes imaged with the miniature microscope during wake (left), NREMS (middle), and REMS (right) under baseline (BL; top row) and sleep-deprived (SD; bottom row) conditions at ZT6 from 119 regions of interest (ROI) from one representative mouse. Bout lengths shown in each matrix are as follows: wake = 20 s, NREMS = 60 s, REMS = 60 s.

(B) Mean (±SEM) Pearson correlation coefficients of ΔF/F values across many astrocytes imaged with the miniature microscope during wake, NREMS, and REMS at ZT6 under BL (closed bars) and SD (open bars) conditions (n = 4 mice; Friedman test).

(C) Individual Pearson correlation coefficients of ΔF/F values from each mouse reported in (B) plotted against their respective p value. Vertical, red, dashed line denotes a p value of 0.05. Data points to the left of this line correspond to significant Pearson correlation coefficients.

(D) Mean (±SEM) number of events that overlap in time within individual astrocytes during wake (W) and NREMS (NR) at ZT6 under BL and SD conditions measured with two-photon microscopy and analyzed with AQuA (BL: n = 27 cells from 4 mice; SD: n = 28 cells from 4 mice). Picture shows cyan event co-occurring with other events in gray within a 9–11 s time period (between states: Wilcoxon signed-rank test; BL versus SD: Mann-Whitney U test).

(E) Mean (±SEM) number of events that overlap in space within individual astrocytes during W and NR at ZT6 under BL and SD conditions captured with two-photon microscopy and analyzed with AQuA (BL: n = 27 cells from 4 mice; SD: n = 28 cells from 4 mice). Heatmap indicates the number of Ca^{2+} events per minute at each location. (Between states: Wilcoxon signed-rank test; BL versus SD: Mann-Whitney U test).

For (B), (D), and (E), *brackets denote comparisons between vigilance states for BL (solid) and for SD (dashed); # denotes comparisons between BL and SD within each vigilance state. $p < 0.05$.

DISCUSSION

We investigated the role of astroglial Ca^{2+} in mammalian sleep. We find that this mediator of astroglial function changes dynamically across sleep and wake and after SD. Reducing the astroglial Ca^{2+} signal *in vivo* also reduces the homeostatic response to SD without altering baseline sleep or patterns of core body temperature or activity. These findings demonstrate that sleep is not only accompanied by widespread activity changes in neurons but also by changes in glial cells. They further suggest that astroglial Ca^{2+} signaling is part of the mammalian sleep homeostat.

Our findings address several important issues in the field of sleep and glial biology. First, they suggest that across the sleep-wake cycle there is a separate level of brain organization (glia) that changes as dynamically as neurons. If true, these findings could fundamentally change our scientific understanding of sleep, because this has been shaped almost entirely by neuron-based studies. One possible explanation for our findings is that changes in astroglial Ca^{2+} are passively driven by changes in surrounding, local neuronal activity. For example, in all vigilance states, most of the astroglial Ca^{2+} signal (as measured by mean ΔF/F and frequency of Ca^{2+} events) was in processes that often surround and respond to changes in local synaptic activity and metabolism [23–26]. On the other hand, astroglial Ca^{2+} did not appear to merely mirror patterns of neuronal activity (reported with electrophysiology [9, 31], but see [35]) characteristic of wake and sleep. For example, wake and REMS display similar levels and patterns of cortical neuron firing [9, 31], but this was not true for astroglial Ca^{2+} activity. In addition, NREMS is typified by highly synchronous neuronal electrical activity compared to wake, and this neuronal synchrony increases further after SD

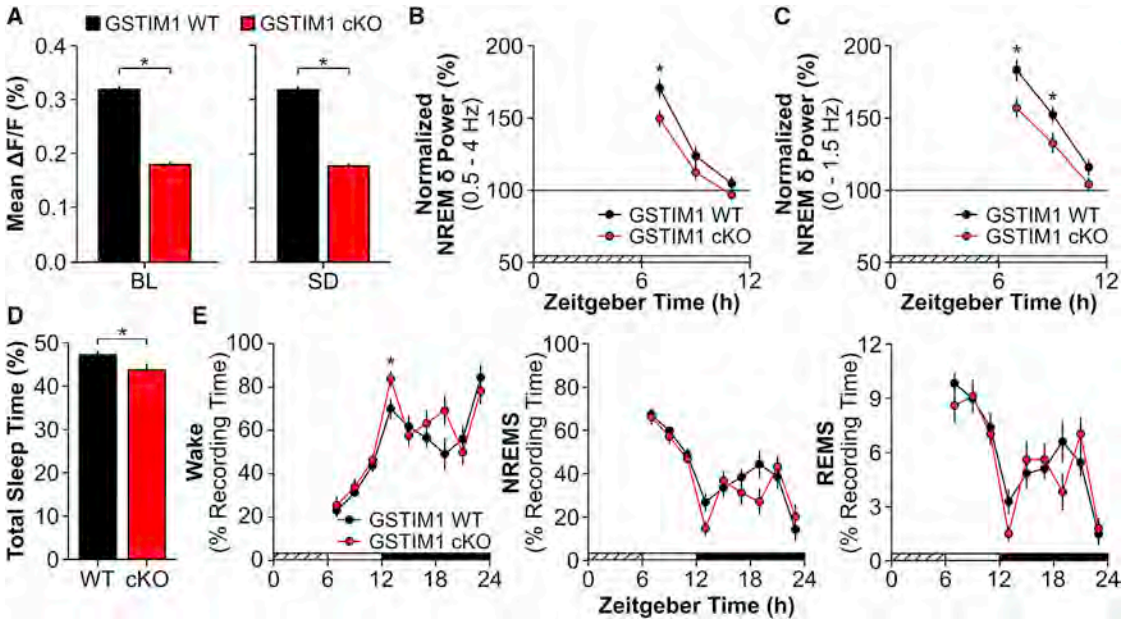

Figure 6. Reductions in Astroglial Ca^{2+} Attenuate Homeostatic Response to Sleep Deprivation

(A) Mean ΔF/F values for GSTIM1 WT (black; n = 3) and GSTIM1 cKO (red; n = 4) at ZT6 under baseline (BL) and sleep-deprived (SD) conditions (Mann-Whitney U test).

(B and C) Normalized NREM δ power (i.e., NREM SWA; 0.5–4 Hz) (B) and normalized low NREM δ power (0–1.5 Hz) (C) during the first 6 h of recovery post-SD averaged across 2 h bins (repeated-measures ANOVA).

(D) Total time spent asleep (sum of NREMS and REMS) during the 18 h recovery phase post-SD expressed as percentage of total recording time for GSTIM1 WT (WT) and GSTIM1 cKO (cKO) (unpaired t test).

(E) Time spent in wake (left), NREMS (middle), and REMS (right) during the 18 h recovery phase post-SD expressed as a percentage of recording time across 2 h bins (repeated-measures ANOVA). Values are means ± SEM. Group means for (B)–(E) are from n = 8 GSTIM1 WT and n = 9 GSTIM1 cKO mice. *Genotypic differences. $p < 0.05$. See also Figures S4–S6.

[9, 31]. In contrast, synchrony of astroglial Ca^{2+} activity was lower during NREMS and reduced even further after SD. If changes in astroglial synchrony were merely driven by neurons, one might expect slower oscillations (due to slower signaling in astrocytes and GCaMP measures versus electrophysiology) but not a reduction in synchrony as shown in Figure 5. In addition, astroglial Ca^{2+} oscillations can occur independently of neuronal activity [36]. Therefore, while we cannot exclude the possibility that the patterns of astrocyte activity we see are partly driven by surrounding neurons, our findings raise the possibility that the regulation and function of sleep may also directly involve glial cells.

Second, our findings support the idea that astrocytes play a role in sleep homeostasis [2]. SD in mammals produces homeostatic and compensatory changes in neurons [31, 37]. We now show that an entirely different class of brain cells also exhibits compensatory changes in response to SD *in vivo*. NREMS Ca^{2+} changes were aligned with the accumulation and discharge of sleep need as measured by NREM SWA. This is notable because the need for sleep is best modeled by changes in NREM SWA [21, 22]. More fine-grained analyses of network and single astrocyte activity further suggest that changes in sleep need manifest in changes in astrocyte activity. More specifically, our findings suggest that increased sleep need increases activity in astroglial processes relative to the soma during sleep (Figure 4), and this increased activity is more prominent in regions furthest from the soma. Indeed, the area and duration of Ca^{2+} activity after SD progressively increased as the activity moved further from the soma and closer to the more distal processes during sleep (Figure S2). These findings are consistent with greater activity in astroglial microdomains as they operate independently from one another and often surround specific subsets of neuronal synapses [19, 38]. Collectively, these results demonstrate that astroglial activity (as measured by Ca^{2+} signals) changes in ways consistent with these cells playing a role in sleep homeostasis. This interpretation is consistent with findings in anesthetized animals, which show that elevated astroglial Ca^{2+} activity can drive slow oscillations in cortical neurons [16].

To more directly test this idea, we showed that conditional reduction of the astroglial Ca^{2+} signal selectively reduced classic measures of sleep homeostasis (NREM SWA and sleep time) without impacting basal sleep and wake expression, core body temperature, or diurnal/nocturnal activity patterns in freely behaving mice. These results indicate that this manipulation specifically impacted sleep homeostasis. Similar results were reported following inducible inhibition of astroglial gliotransmission, particularly in the lower SWA bands that are most sensitive to sleep loss [2]. These findings suggest that changes in astroglial intracellular Ca^{2+} encode sleep need and trigger feedback onto neurons perhaps via gliotransmission of ATP [24], which is hydrolyzed to the sleep-inducing molecule adenosine [2].

Third, our analyses may reveal different ways astrocytes respond to neural inputs across different vigilance states. Under baseline conditions, Ca^{2+} signaling was highly synchronized across astrocytes, but this synchrony was most pronounced during waking, a brain state characterized by high concentrations of excitatory neuromodulators like noradrenaline. Noradrenaline and other excitatory neuromodulators are released throughout the neocortex [39] and can trigger widespread astroglial activation that encompasses the entire cell [40, 41]. Conversely, astroglial network synchrony was lowest in sleep, which is when the release of noradrenaline is at a nadir [39]. State-dependent shifts in noradrenaline concentrations (i.e., highest in wake, lowest in REMS) may also explain why astroglial Ca^{2+} activity is highest in wake and lowest in REMS. Additionally, changes in noradrenaline may drive the dramatic increase in astroglial Ca^{2+} signaling during REMS-to-wake transitions, as the latter would be accompanied by a sharp increase in cortical noradrenaline concentrations [42].

Our findings also address an ongoing controversy in the field of glial biology. Astroglial Ca^{2+} dynamically changes in response to neurotransmitters, metabolic signals, and mechanical stimulation [43–45]. Studies *in vitro* have also shown that increases in Ca^{2+} trigger gliotransmission [46, 47]. Yet, previous manipulations of intracellular astroglial Ca^{2+} *in vivo* do not always reveal significant behavioral phenotypes [48]. We used a novel approach to this problem (GSTIM1 cKO mice) that targeted a rate-limiting step in endoplasmic reticulum replenishment of astroglial intracellular Ca^{2+}. We find that this manipulation reduces the homeostatic response to SD, thus demonstrating a functional role for astroglial Ca^{2+} in a complex, regulated brain process *in vivo*.

Future Directions and Unanswered Questions

We show that astrocytes dynamically change their activity across the sleep-wake cycle and in response to SD. These findings support the idea that astrocytes play an important role in mammalian sleep, but they raise many questions. For example, while our studies demonstrate that astroglial intracellular Ca^{2+} influences sleep homeostasis, the precise sites and mechanisms of action are unknown. Astrocytes enwrap neurons in areas most sensitive to sleep need (e.g., frontal cortical neurons) as well as many canonical sleep and wake executive circuits [15, 49]. Increases in intracellular Ca^{2+} trigger gliotransmission of ATP [50], which is hydrolyzed to the sleep-inducing molecule adenosine. It is therefore possible that the rise in intracellular Ca^{2+} during wakefulness leads to greater gliotransmission and increased sleep drive, a process reversed during sleep [51]. Such a mechanism could theoretically influence "local" sleep within the cortex as well as global changes in sleep behavior via action in canonical sleep and wake executive circuits, but this remains to be determined [1]. Additionally, previous studies reported that different sources of Ca^{2+} are used by astroglial somata (e.g., endoplasmic reticulum stores) and processes (e.g., TRP or ion channels) [43]. Since our current studies highlight the diversity of subcellular Ca^{2+} activity in astrocytes, future studies are needed to determine how various Ca^{2+} sources are impacted by SD and, more broadly, how they contribute to the spatiotemporal diversity of astroglial Ca^{2+} signals. Future studies are also needed to determine the functions of sleep-wake dependent changes in astroglial activity. We show that, during sleep, astroglial activity (as measured by intracellular Ca^{2+}) is biased toward the distal processes. As distal processes form discrete microdomains around sets of synapses, this suggests that astrocytes influence synaptic plasticity during sleep. While speculative, this idea is supported by the strong association between sleep and plasticity [52] and findings implicating astrocytes and other glia in various forms of synaptic remodeling [53]. While the manuscript was in review, supporting findings were published by Bojarskaite et al. [54].

STAR★METHODS

Detailed methods are provided in the online version of this paper and include the following:

- KEY RESOURCES TABLE
- RESOURCE AVAILABILITY
  - Lead Contact
  - Materials Availability
  - Data and Code Availability
- EXPERIMENTAL MODEL AND SUBJECT DETAILS
  - Mice
- METHOD DETAILS
  - Surgical procedures
  - EEG & EMG implantation for sleep phenotyping
  - Telemeter implantation for activity & temperature
  - Tamoxifen injections
  - Immunofluorescence
- EXPERIMENTAL DESIGN
  - Ca^{2+} imaging with EEG & EMG recording
  - GSTIM1 response to methoxamine
  - GSTIM1 sleep phenotyping
  - GSTIM1 patterns in activity & core temperature
  - Miniature microscope imaging with EEG & EMG
  - Data processing and analysis
  - Two-photon imaging with EEG & EMG
  - Data processing and analysis
  - Sleep phenotyping
- QUANTIFICATION AND STATISTICAL ANALYSIS

SUPPLEMENTAL INFORMATION

Supplemental Information can be found online at https://doi.org/10.1016/j.cub.2020.08.052.

ACKNOWLEDGMENTS

We thank Taylor Wintler and Hannah Schoch for assisting with sleep deprivation. We also thank Will Clegern for engineering and fabricating custom hardware for imaging and Eric Marr for assistance with analysis. We thank Mark Wu for discussions of unpublished results. This work was funded by NIH grants F32 NS100335 (A.M.I.), R01 MH099544 and R01 NS114780 (M.G.F.), R01 NS078498 (J.P.W. and M.J.R.), and R03 DA042480 (C.R.H. and M.G.F.).

AUTHOR CONTRIBUTIONS

Conceptualization, A.M.I. and M.G.F.; Methodology, A.M.I. and M.G.F.; Investigation, A.M.I. and K.G.S.; Software, A.M.I., C.R.H., D.O.H., J.P.W., and M.J.R.; Formal Analysis, A.M.I., C.R.H., D.O.H., J.P.W., M.J.R., and M.G.F., Resources, J.P.W. and M.G.F.; Writing – Original Draft, A.M.I., C.R.H.,

D.O.H., and M.G.F. Writing – Review & Editing, A.M.I., C.R.H., D.O.H., K.G.S., M.J.R., J.P.W., and M.G.F.

DECLARATION OF INTERESTS

The authors declare no competing interests.

Received: January 17, 2020
Revised: July 7, 2020
Accepted: August 13, 2020
Published: September 24, 2020

REFERENCES

1. Frank, M.G. (2019). The role of glia in sleep regulation and function. Handb. Exp. Pharmacol. *253*, 83–96.
2. Halassa, M.M., Florian, C., Fellin, T., Munoz, J.R., Lee, S.Y., Abel, T., Haydon, P.G., and Frank, M.G. (2009). Astrocytic modulation of sleep homeostasis and cognitive consequences of sleep loss. Neuron *61*, 213–219.
3. Halassa, M.M., Fellin, T., and Haydon, P.G. (2007). The tripartite synapse: roles for gliotransmission in health and disease. Trends Mol. Med. *13*, 54–63.
4. Fellin, T., Pascual, O., and Haydon, P.G. (2006). Astrocytes coordinate synaptic networks: balanced excitation and inhibition. Physiology (Bethesda) *21*, 208–215.
5. Araque, A. (2008). Astrocytes process synaptic information. Neuron Glia Biol. *4*, 3–10.
6. Briggs, C., Hirasawa, M., and Semba, K. (2018). Sleep deprivation distinctly alters glutamate transporter 1 apposition and excitatory transmission to orexin and MCH neurons. J. Neurosci. *38*, 2505–2518.
7. O'Donnell, J., Ding, F., and Nedergaard, M. (2015). Distinct functional states of astrocytes during sleep and wakefulness: Is norepinephrine the master regulator? Curr. Sleep Med. Rep. *1*, 1–8.
8. Foley, J., Blutstein, T., Lee, S., Erneux, C., Halassa, M.M., and Haydon, P. (2017). Astrocytic IP3/Ca2+ signaling modulates theta rhythm and REM sleep. Front. Neural Circuits *11*, 3.
9. Steriade, M. (2000). Corticothalamic resonance, states of vigilance and mentation. Neuroscience *101*, 243–276.
10. Pelayo, R., and Dement, W.C. (2017). History of sleep physiology and medicine. In Principles and Practice of Sleep Medicine, Sixth Edition, M. Kryger, T. Roth, and W.C. Dement, eds. (Elsevier), pp. 3–14.
11. Kleitman, N. (1963). Sleep and Wakefulness (Univ. Chicago Press).
12. Drucker-Colin, R., and Merchant-Nancy, H. (1995). The Pharmacology of Sleep, First Edition (Springer-Verlag).
13. Bellesi, M., de Vivo, L., Chini, M., Gilli, F., Tononi, G., and Cirelli, C. (2017). Sleep loss promotes astrocytic phagocytosis and microglial activation in mouse cerebral cortex. J. Neurosci. *37*, 5263–5273.
14. Bellesi, M., Pfister-Genskow, M., Maret, S., Keles, S., Tononi, G., and Cirelli, C. (2013). Effects of sleep and wake on oligodendrocytes and their precursors. J. Neurosci. *33*, 14288–14300.
15. Bellesi, M., de Vivo, L., Tononi, G., and Cirelli, C. (2015). Effects of sleep and wake on astrocytes: clues from molecular and ultrastructural studies. BMC Biol. *13*, 66.
16. Poskanzer, K.E., and Yuste, R. (2016). Astrocytes regulate cortical state switching in vivo. Proc. Natl. Acad. Sci. USA *113*, E2675–E2684.
17. Tobler, I. (2005). Phylogeny of sleep regulation. In Principles and Practice of Sleep Medicine, 4th Edition, M.H. Kryger, T. Roth, and W.C. Dement, eds. (Elsevier Saunders), pp. 77–90.
18. Bjorness, T.E., Dale, N., Mettlach, G., Sonneborn, A., Sahin, B., Fienberg, A.A., Yanagisawa, M., Bibb, J.A., and Greene, R.W. (2016). An adenosine-mediated glial-neuronal circuit for homeostatic sleep. J. Neurosci. *36*, 3709–3721.
19. Khakh, B.S., and McCarthy, K.D. (2015). Astrocyte calcium signaling: from observations to functions and the challenges therein. Cold Spring Harb. Perspect. Biol. *7*, a020404.
20. Franken, P., Lopez-Molina, L., Marcacci, L., Schibler, U., and Tafti, M. (2000). The transcription factor DBP affects circadian sleep consolidation and rhythmic EEG activity. J. Neurosci. *20*, 617–625.
21. Borbély, A.A., and Achermann, P. (1999). Sleep homeostasis and models of sleep regulation. J. Biol. Rhythms *14*, 557–568.
22. Franken, P., Tobler, I., and Borbély, A.A. (1991). Sleep homeostasis in the rat: simulation of the time course of EEG slow-wave activity. Neurosci. Lett. *130*, 141–144.
23. Srinivasan, R., Huang, B.S., Venugopal, S., Johnston, A.D., Chai, H., Zeng, H., Golshani, P., and Khakh, B.S. (2015). Ca(2+) signaling in astrocytes from Ip3r2(-/-) mice in brain slices and during startle responses in vivo. Nat. Neurosci. *18*, 708–717.
24. Perea, G., Navarrete, M., and Araque, A. (2009). Tripartite synapses: astrocytes process and control synaptic information. Trends Neurosci. *32*, 421–431.
25. Khakh, B.S., and Sofroniew, M.V. (2015). Diversity of astrocyte functions and phenotypes in neural circuits. Nat. Neurosci. *18*, 942–952.
26. Stobart, J.L., Ferrari, K.D., Barrett, M.J.P., Glück, C., Stobart, M.J., Zuend, M., and Weber, B. (2018). Cortical circuit activity evokes rapid astrocyte calcium signals on a similar timescale to neurons. Neuron *98*, 726–735.
27. Guerra-Gomes, S., Sousa, N., Pinto, L., and Oliveira, J.F. (2018). Functional roles of astrocyte calcium elevations: from synapses to behavior. Front. Cell. Neurosci. *11*, 427.
28. Wang, Y., DelRosso, N.V., Vaidyanathan, T.V., Cahill, M.K., Reitman, M.E., Pittolo, S., Mi, X., Yu, G., and Poskanzer, K.E. (2019). Accurate quantification of astrocyte and neurotransmitter fluorescence dynamics for single-cell and population-level physiology. Nat. Neurosci. *22*, 1936–1944.
29. Franken, P., Chollet, D., and Tafti, M. (2001). The homeostatic regulation of sleep need is under genetic control. J. Neurosci. *21*, 2610–2621.
30. Koizumi, S. (2010). Synchronization of Ca2+ oscillations: involvement of ATP release in astrocytes. FEBS J. *277*, 286–292.
31. Vyazovskiy, V.V., Olcese, U., Lazimy, Y.M., Faraguna, U., Esser, S.K., Williams, J.C., Cirelli, C., and Tononi, G. (2009). Cortical firing and sleep homeostasis. Neuron *63*, 865–878.
32. Moreno, C., Sampieri, A., Vivas, O., Peña-Segura, C., and Vaca, L. (2012). STIM1 and Orai1 mediate thrombin-induced Ca(2+) influx in rat cortical astrocytes. Cell Calcium *52*, 457–467.
33. Szmigielski, A., and Górska, D. (1997). The effect of prolonged imipramine treatment on the alpha 1-adrenoceptor-induced translocation of protein kinase C in the central nervous system in rats. Pharmacol. Res. *35*, 569–576.
34. Ding, F., O'Donnell, J., Thrane, A.S., Zeppenfeld, D., Kang, H., Xie, L., Wang, F., and Nedergaard, M. (2013). α1-Adrenergic receptors mediate coordinated Ca2+ signaling of cortical astrocytes in awake, behaving mice. Cell Calcium *54*, 387–394.
35. Niethard, N., Ngo, H.-V.V., Ehrlich, I., and Born, J. (2018). Cortical circuit activity underlying sleep slow oscillations and spindles. Proc. Natl. Acad. Sci. USA *115*, E9220–E9229.
36. Nett, W.J., Oloff, S.H., and McCarthy, K.D. (2002). Hippocampal astrocytes in situ exhibit calcium oscillations that occur independent of neuronal activity. J. Neurophysiol. *87*, 528–537.
37. Borbely, A.A., and Achermann, P. (2000). Sleep homeostasis and models of sleep regulation. In Principles and Practice of Sleep Medicine, Third Edition, M. Kryger, T. Roth, and W.C. Dement, eds. (Saunders), pp. 377–390.
38. Shigetomi, E., Bushong, E.A., Haustein, M.D., Tong, X., Jackson-Weaver, O., Kracun, S., Xu, J., Sofroniew, M.V., Ellisman, M.H., and Khakh, B.S. (2013). Imaging calcium microdomains within entire astrocyte territories and endfeet with GCaMPs expressed using adeno-associated viruses. J. Gen. Physiol. *141*, 633–647.

39. Jones, B.E. (2005). From waking to sleeping: neuronal and chemical substrates. Trends Pharmacol. Sci. *26*, 578–586.

40. Kjaerby, C., Rasmussen, R., Andersen, M., and Nedergaard, M. (2017). Does global astrocytic calcium signaling participate in awake brain state transitions and neuronal circuit function? Neurochem. Res. *42*, 1810–1822.

41. Mu, Y., Bennett, D.V., Rubinov, M., Narayan, S., Yang, C.-T., Tanimoto, M., Mensh, B.D., Looger, L.L., and Ahrens, M.B. (2019). Glia accumulate evidence that actions are futile and suppress unsuccessful behavior. Cell *178*, 27–43.

42. Jones, B. (2009). Sleep–wake state regulation by noradrenaline and serotonin. In Encyclopedia of Neuroscience, L.R. Squire, ed. (Academic Press, Elsevier), pp. 1079–1083.

43. Bazargani, N., and Attwell, D. (2016). Astrocyte calcium signaling: the third wave. Nat. Neurosci. *19*, 182–189.

44. Oheim, M., Schmidt, E., and Hirrlinger, J. (2018). Local energy on demand: Are 'spontaneous' astrocytic Ca^{2+}-microdomains the regulatory unit for astrocyte-neuron metabolic cooperation? Brain Res. Bull. *136*, 54–64.

45. Fujii, Y., Maekawa, S., and Morita, M. (2017). Astrocyte calcium waves propagate proximally by gap junction and distally by extracellular diffusion of ATP released from volume-regulated anion channels. Sci. Rep. *7*, 13115.

46. Fiacco, T.A., and McCarthy, K.D. (2018). Multiple lines of evidence indicate that gliotransmission does not occur under physiological conditions. J. Neurosci. *38*, 3–13.

47. Savtchouk, I., and Volterra, A. (2018). Gliotransmission: Beyond Black-and-White. J. Neurosci. *38*, 14–25.

48. Petravicz, J., Boyt, K.M., and McCarthy, K.D. (2014). Astrocyte IP3R2-dependent Ca(2+) signaling is not a major modulator of neuronal pathways governing behavior. Front. Behav. Neurosci. *8*, 384.

49. Pelluru, D., Konadhode, R.R., Bhat, N.R., and Shiromani, P.J. (2016). Optogenetic stimulation of astrocytes in the posterior hypothalamus increases sleep at night in C57BL/6J mice. Eur. J. Neurosci. *43*, 1298–1306.

50. Lee, J., Chun, Y.E., Han, K.S., Lee, J., Woo, D.H., and Lee, C.J. (2015). Ca(2+) entry is required for mechanical stimulation-induced ATP release from astrocyte. Exp. Neurobiol. *24*, 17–23.

51. Frank, M.G. (2013). Astroglial regulation of sleep homeostasis. Curr. Opin. Neurobiol. *23*, 812–818.

52. Seibt, J., and Frank, M.G. (2019). Primed to sleep: the dynamics of synaptic plasticity across brain states. Front. Syst. Neurosci. *13*, 2.

53. Allen, N.J., and Eroglu, C. (2017). Cell biology of astrocyte-synapse interactions. Neuron *96*, 697–708.

54. Bojarskaite, L., Bjørnstad, D.M., Pettersen, K.H., Cunen, C., Hermansen, G.H., Åbjørsbråten, K.S., Chambers, A.R., Sprengel, R., Vervaeke, K., Tang, W., et al. (2020). Astrocytic Ca^{2+} signaling is reduced during sleep and is involved in the regulation of slow wave sleep. Nat. Commun. *11*, 3240.

55. Schneider, C.A., Rasband, W.S., and Eliceiri, K.W. (2012). NIH Image to ImageJ: 25 years of image analysis. Nat. Methods *9*, 671–675.

56. Schindelin, J., Arganda-Carreras, I., Frise, E., Kaynig, V., Longair, M., Pietzsch, T., Preibisch, S., Rueden, C., Saalfeld, S., Schmid, B., et al. (2012). Fiji: an open-source platform for biological-image analysis. Nat. Methods *9*, 676–682.

57. R Core Team (2017). R: A language and environment for statistical computing. R Foundation for Statistical Computing, Vienna, Austria, https://www.R-project.org/.

58. Heuser, K., Nome, C.G., Pettersen, K.H., Åbjørsbråten, K.S., Jensen, V., Tang, W., Sprengel, R., Taubøll, E., Nagelhus, E.A., and Enger, R. (2018). Ca^{2+} signals in astrocytes facilitate spread of epileptiform activity. Cereb. Cortex *28*, 4036–4048.

59. Frank, M.G., Stryker, M.P., and Tecott, L.H. (2002). Sleep and sleep homeostasis in mice lacking the 5-HT2c receptor. Neuropsychopharmacology *27*, 869–873.

60. Ingiosi, A.M., Schoch, H., Wintler, T., Singletary, K.G., Righelli, D., Roser, L.G., Medina, E., Risso, D., Frank, M.G., and Peixoto, L. (2019). Shank3 modulates sleep and expression of circadian transcription factors. eLife *8*, e42819.

61. Huber, R., Deboer, T., and Tobler, I. (2000). Effects of sleep deprivation on sleep and sleep EEG in three mouse strains: empirical data and simulations. Brain Res. *857*, 8–19.

62. Tobler, I., Deboer, T., and Fischer, M. (1997). Sleep and sleep regulation in normal and prion protein-deficient mice. J. Neurosci. *17*, 1869–1879.

63. Ingiosi, A.M., Raymond, R.M., Jr., Pavlova, M.N., and Opp, M.R. (2015). Selective contributions of neuronal and astroglial interleukin-1 receptor 1 to the regulation of sleep. Brain Behav. Immun. *48*, 244–257.

64. Gulati, S., Cao, V.Y., and Otte, S. (2017). Multi-layer Cortical Ca2+ Imaging in Freely Moving Mice with Prism Probes and Miniaturized Fluorescence Microscopy. JoVE, e55579.

65. Adamantidis, A.R., Zhang, F., Aravanis, A.M., Deisseroth, K., and de Lecea, L. (2007). Neural substrates of awakening probed with optogenetic control of hypocretin neurons. Nature *450*, 420–424.

66. Weber, F., Hoang Do, J.P., Chung, S., Beier, K.T., Bikov, M., Saffari Doost, M., and Dan, Y. (2018). Regulation of REM and non-REM sleep by periaqueductal GABAergic neurons. Nat. Commun. *9*, 354.

67. Jimenez, J.C., Su, K., Goldberg, A.R., Luna, V.M., Biane, J.S., Ordek, G., Zhou, P., Ong, S.K., Wright, M.A., Zweifel, L., et al. (2018). Anxiety cells in a hippocampal-hypothalamic circuit. Neuron *97*, 670–683.

68. Kirschen, G.W., Shen, J., Tian, M., Schroeder, B., Wang, J., Man, G., Wu, S., and Ge, S. (2017). Active dentate granule cells encode experience to promote the addition of adult-born hippocampal neurons. J. Neurosci. *37*, 4661–4678.

69. Resendez, S.L., Jennings, J.H., Ung, R.L., Namboodiri, V.M., Zhou, Z.C., Otis, J.M., Nomura, H., McHenry, J.A., Kosyk, O., and Stuber, G.D. (2016). Visualization of cortical, subcortical and deep brain neural circuit dynamics during naturalistic mammalian behavior with head-mounted microscopes and chronically implanted lenses. Nat. Protoc. *11*, 566–597.

70. Eban-Rothschild, A., Rothschild, G., Giardino, W.J., Jones, J.R., and de Lecea, L. (2016). VTA dopaminergic neurons regulate ethologically relevant sleep-wake behaviors. Nat. Neurosci. *19*, 1356–1366.

71. Paukert, M., Agarwal, A., Cha, J., Doze, V.A., Kang, J.U., and Bergles, D.E. (2014). Norepinephrine controls astroglial responsiveness to local circuit activity. Neuron *82*, 1263–1270.

72. Oike, H., Ogawa, Y., and Oishi, K. (2019). Simple and quick visualization of periodical data using microsoft excel. Methods Protoc. *2*, 81.

STAR★METHODS

KEY RESOURCES TABLE

REAGENT or RESOURCE	SOURCE	IDENTIFIER
Antibodies		
Mouse anti-GFAP	Cell Signaling Technology	Cat# 3670; RRID: AB_561049
Mouse anti-NeuN	Millipore	Cat# MAB377; RRID: AB_2298772
Biotinylated horse anti-mouse	Vector Laboratories	Cat# BA-2000; RRID: AB_2313581
Texas Red streptavidin	Vector Laboratories	Cat# SA-1200; RRID: AB_2336464
Chicken anti-beta galactosidase	Abcam	Cat# ab9361; RRID: AB_307210
Rabbit anti-S100β	Abcam	Cat# ab52642; RRID: AB_882426
Goat anti-chicken 488	Abcam	Cat# ab150169; RRID: AB_2636803
Donkey anti-rabbit 594	Abcam	Cat# ab150076; RRID: AB_2782993
Goat anti-mouse 594	Abcam	Cat# A-21125; RRID: AB_2535767
Bacterial and Virus Strains		
AAV5.GfaABC1D.cytoGCaMP6f.SV40	Penn Vector Core	Cat# AV-5-52925; Custom preparation
Chemicals, Peptides, and Recombinant Proteins		
Tamoxifen	Sigma-Aldrich	Cat# T5648; CAS: 10540-29-1
Sunflower oil	Sigma-Aldrich	Cat# S5007; CAS: 8001-21-6
Methoxamine hydrochloride	Sigma-Aldrich	Cat# M6524; CAS: 61-16-5
Experimental Models: Organisms/Strains		
Mouse: C57BL/6J	The Jackson Laboratory	JAX: 000664; RRID: IMSR_JAX:000664
Mouse: B6.Cg-Tg(GFAP-cre/ERT2)505Fmv/J	The Jackson Laboratory	JAX: 012849; RRID: IMSR_JAX:012849
Mouse: B6(Cg)-Stim1^{tm1Rao}/J	The Jackson Laboratory	JAX: 023350; RRID: IMSR_JAX:023350
Mouse: FVB.129S4(B6)-Gt(ROSA)26Sor^{tm1Sor}/J	The Jackson Laboratory	JAX: 009427: RRID: IMSR_JAX:009427
Software and Algorithms		
Sirenia Acquisition v1.7.7	Pinnacle Technologies	https://www.pinnaclet.com/
nVista HD v2.0.4	Inscopix	https://inscopix.com
Data Processing Software v1.2.1	Inscopix	https://inscopix.com
OpenEx	Tucker-Davis Technologies	https://www.tdt.com/
Prairie View	Bruker	https://www.bruker.com/
ImageJ	[55]	https://imagej.nih.gov/ij/
Fiji	[56]	https://imagej.net/Fiji
VitalRecorder v3,0,0,0	Kissei Comtec Co., LTD	http://www.sleepsign.com/
SleepSign for Animal v3,0,0,812	Kissei Comtec Co., LTD	http://www.sleepsign.com/
Running Wheel Manager Data Acquisition Software	Med Associates Inc.	Cat# SOF-860; https://www.med-associates.com/
VitalView Telemetry Data Acquisition Software	Starr Life Sciences Corp.	https://www.starrlifesciences.com/
Astrocyte Quantitative Analysis	[28]	https://github.com/yu-lab-vt/aqua
SigmaPlot v11.0	Systat Software, Inc	https://systatsoftware.com/products/sigmaplot/
SPSS for Windows 25	IBM	https://www.ibm.com/analytics/academic-statistics-software
R v3.6.0	[57]	https://www.r-project.org/
Aligning and processing algorithm	This paper	Available upon request

RESOURCE AVAILABILITY

Lead Contact

Further information and requests for resources and reagents should be directed to and will be fulfilled by the Lead Contact, Marcos G. Frank (marcos.frank@wsu.edu).

Materials Availability

This study did not generate new unique reagents.

Data and Code Availability

The code generated for this study will be available upon request from the Lead Contact (Marcos G. Frank, marcos.frank@wsu.edu).

EXPERIMENTAL MODEL AND SUBJECT DETAILS

Mice

C57BL/6J (#000664), B6.Cg-Tg(GFAP-cre/ERT2)505Fmv/J (GFAP-Cre/ERT2; #012849), B6(Cg)-Stim1^{tm1Rao}/J (STIM1$^{fl/fl}$; #023350), and FVB.129S4(B6)-Gt(ROSA)26Sor^{tm1Sor}/J (R26R$^{fl/fl}$; #009427) mice were obtained from The Jackson Laboratory (Bar Harbor, ME). Breeding pairs of hemizygous GFAP-Cre/ERT2$^{Tg+/-}$ and homozygous STIM1$^{fl/fl}$ were established to obtain GFAP-Cre/ERT2$^{-/-}$; STIM1$^{fl/fl}$ wild-type mice (GSTIM1 WT) and GFAP-Cre/ERT2$^{Tg+/-}$;STIM1$^{fl/fl}$ conditional knockout (GSTIM1 cKO) mutant mice. Breeding pairs of hemizygous GFAP-Cre/ERT2$^{Tg+/-}$ and homozygous R262R$^{fl/fl}$ were established to obtain GFAP-Cre/ERT2$^{-/-}$;R26R$^{fl/fl}$ wild-type (GR26R WT) mice and GFAP-Cre/ERT2$^{Tg+/-}$;R26R$^{fl/fl}$ conditional knockout (GR26R cKO) mice. Genotyping of GSTIM1 WT, GSTIM1 cKO, GR26R WT, and GR26R cKO mice was completed prior to experiments by Transnetyx, Inc (Cordova, TN). Mice were housed in standard cages on 24 ± 1°C on a 12:12 h light:dark cycle with food and water *ad libitum*. Details regarding the number, age, and sex of mice used are provided below. All experimental procedures were approved by the Institutional Animal Care and Use Committee of Washington State University and conducted in accordance with National Research Council guidelines and regulations for experiments in live animals.

METHOD DETAILS

Surgical procedures

Ca^{2+} imaging with EEG & EMG recording

Adult male mice [for miniature microscope: n = 6 C57BL/6J, n = 6 GSTIM1 WT, n = 8 GSTIM1 cKO; for two-photon microscope: n = 4 C57BL/6J; 8 – 14-weeks-old] were anesthetized using isoflurane and placed in a stereotaxic frame. A 3-mm craniotomy was made over the frontal cortex leaving the dura intact. AAV2/5 *GfaABC$_1$D*-GCaMP6f (3.31×10^{13} GC/ml; Penn Vector Core, Philadelphia, PA) was injected at two adjacent sites (AP: 2.0 – 2.5 mm, ML: −1.25 – −1.75 mm, DV: −0.18 – −0.20 mm) in the frontal cortex. 1.5 μl of vector was injected at each site at 200 nl/min. The needle remained in place for 10 min after the injection was complete. After vector delivery, a 3-mm glass coverslip was fixed over the craniotomy with cyanoacrylate adhesive. For electrode implantation, four 0.5-mm diameter holes were drilled in the skull unilaterally over frontal, somatosensory, and occipital cortices in the hemisphere contralateral to the AAV2/5 *GfaABC$_1$D*-GCaMP6f injection site. Sterilized stainless steel EEG electrodes were inserted into these holes just under the skull, and 2 additional EMG electrodes were placed into the nuchal muscles. Cranial electrodes were secured with dental acrylic. For two-photon imaging, a custom-milled head-restraint bar was then fixed to the skull with dental acrylic mixed with black carbon powder. Mice were imaged 2 – 4 weeks later to allow time for the fluorescent indicator to be expressed [23, 58].

For imaging with the head-mounted miniature microscope, mice were fitted with a baseplate 1.5 – 2.5 weeks after surgery under isoflurane anesthesia. The baseplate used to house the miniature microscope was secured with dental acrylic mixed with black carbon powder.

EEG & EMG implantation for sleep phenotyping

Adult male and female mice [GSTIM1 WT (n = 8; females = 1) and GSTIM1 cKO (n = 9; females = 4); 10 – 14-weeks-old] were stereotaxically implanted with EEG & EMG electrodes under isoflurane anesthesia according to previously published methods [59, 60]. Briefly, four stainless steel screw electrodes (BC-002MPU188, Bellcan International Corp, Hialeah, FL) were placed contralaterally over frontal (2) and parietal (2) cortices, and 2 EMG electrodes were inserted in the nuchal muscles. Mice were allowed 5 days of recovery from surgery prior to habituation to the recording environment.

Telemeter implantation for activity & temperature

Adult male and female mice [GSTIM WT (n = 3; female = 0) and GSTIM1 cKO (n = 3; female = 1); 15 – 16-weeks-old] were implanted with a telemetry device (G2 E-mitter, STARR Life Sciences Corp., Oakmont, PA) in the peritoneal cavity under isoflurane anesthesia. The telemeter was secured to the abdominal musculature with a suture. The skin was closed with wound clips which were removed after 8 days. During this recovery period, body weight, hydration, and fecal output were monitored daily.

Tamoxifen injections

Prior to all surgical procedures in GSTIM1 WT and GSTIM1 cKO mice, these mice were first injected with tamoxifen (180 mg/kg; #T5648, Sigma-Aldrich, St. Louis, MO) intraperitoneally once per day for 5 consecutive days alternating sides [18]. Tamoxifen was made up at 30 mg/ml in 90% sunflower oil (#S5007, Sigma-Aldrich) with 10% ethanol and sterile filtered through a 0.22 μm filter [18]. All mice received 1 mL lactated Ringer's solution with 5% dextrose subcutaneously daily until mice started regaining body weight. Surgical procedures were performed no sooner than 10 days after the final tamoxifen injection when mice regained body

weight. This same injection procedure was followed for GR26R WT and GR26R cKO mice prior to tissue collection for immunofluorescence (see below).

Immunofluorescence

C57BL/6J mice (n = 2 males; 12-weeks-old) expressing GCaMP6f in cortex were transcardially perfused with 1x phosphate buffered saline (PBS) followed by 10% buffered formalin. Brains were extracted and placed in 30% sucrose in PBS for 24 – 48 h. Brains were frozen in −50°C 2-methylbutane and stored at −80°C until processing. Brains were sectioned coronally at 25 μm on a cryostat. Native green fluorescent protein (GFP) signal from GCaMP6f expression was assessed, and sections were also counterstained for astrocytes and neurons using immunofluorescent techniques. Sections were washed 3 × 15 min in PBS and then incubated overnight at room temperature with primary antibodies against astrocytes (1:1000; mouse anti-GFAP, #3670, Cell Signaling Technology, Danvers, MA) or neurons (1:100; mouse anti-NeuN, #MAB377, Millipore, Burlington, MA) in 1x PBS with 0.3% Triton-X (PBSt). The next day, sections were washed 3 × 10 min in PBS and then incubated for 1.5 h at room temperature with biotinylated horse anti-mouse secondary antibody (1:1000; #BA-2000, Vector Laboratories, Burlingame, CA) in PBSt. Sections were again washed for 3 × 10 min in PBS and then incubated for 2 h at room temperature in Texas Red streptavidin (1:500; #SA-1200, Vector Laboratories) in PBSt. After 3 × 10 min washes in PBS, sections were mounted on slides for imaging.

GR26R WT (n = 3) and GR26R cKO (n = 3) male mice were treated with tamoxifen as described above. Mice were then transcardially perfused with 1x PBS followed by 10% buffered formalin 21 days after the last tamoxifen injection. Brains removed and serially post-fixed for 5 days in solutions of 10% buffered formalin containing 10%, 20%, and 30% sucrose. Brains were frozen in −50°C 2-methylbutane and stored at −80°C until processing. Brains were sectioned sagittally at 25 μm on a cryostat. Sections were then incubated in protein blocking solution containing 1% bovine serum albumin fraction V (#10735094001, Sigma-Aldrich) and 0.1% Triton X-100 (#X100, Sigma-Aldrich) in 1x PBS containing primary antibodies. Brain sections were incubated for 40 h at 25°C on a gentle rocker with the following primary antibodies (1:500): chicken anti-beta galactosidase (#ab9361, Abcam, Cambridge, MA), rabbit anti-S100β (#ab52642, Abcam), and mouse anti-NeuN clone A60 (#mab377, Millipore). These primary antibodies were contrasted using the following secondary antibodies, respectively, used at 1:1500 for 2 h at 25°C on a gentle rocker: goat anti-chicken 488 (#ab150169, Abcam), donkey anti-rabbit 594 (#ab150076, Abcam), and goat anti-mouse 594 (#A-21125, ThermoFisher Scientific, Waltham, MA). Brain sections were then mounted on slides for imaging.

EXPERIMENTAL DESIGN

Ca^{2+} imaging with EEG & EMG recording

Adult male C57BL/6J mice underwent a counterbalanced design of 24 h undisturbed baseline sleep and 6 h SD via gentle handling followed by 18 h recovery sleep to account for potential order effects of imaging over multiple days. For epifluorescent imaging with the miniature microscope (n = 6), EEG & EMG were continuously recorded, and imaging occurred at zeitgeber times (ZT) of high (ZT0) and low (ZT6 and ZT12) sleep need. At ZT0 and ZT12, images were acquired during a 2-min imaging session every 20 min. At ZT6, our primary analysis time point, images were acquired during 2 – 7 min imaging sessions at varying intervals to capture all vigilance states and state transitions. For two-photon microscopy using a different group of mice (n = 4), imaging and EEG & EMG recordings occurred at ZT6 and ZT12 during 3-min imaging sessions at varying intervals to capture all vigilance states. During imaging experiments, vigilance states were determined by visual inspection of the EEG & EMG signals in real time. While in head-restraint in the air-lifted cage, mice spent sustained periods of time (> 20 s) in a 'transitional' or 'intermediate' state characterized by high amplitude, high frequency EEG signals and low amplitude EMG signals. This state was preceded by NREMS but followed by either NREMS, REMS, or wake. This state, as measured by cortical EEG, was not observed in freely behaving animals and seemed to be an artifact of head-restraint conditions. Therefore, Ca^{2+} data collected during this state were not included in analyses as this atypical state is not representative of physiological sleep-wake behavior in mice [61, 62]. For epifluorescent imaging in GSTIM1 mice (n = 3 GSTIM1 WT males; n = 4 GSTIM1 cKO males), EEG & EMG recordings occurred continuously during a 24 h undisturbed baseline day followed by 6 h SD via gentle handling and 18 h recovery sleep. Ca^{2+} imaging occurred at ZT0, 6, and 12 as described for C57BL/6J mice.

GSTIM1 response to methoxamine

Male and female GSTIM WT (n = 3; female = 2) and GSTIM1 cKO (n = 4; female = 2) adult mice (13-weeks-old) were injected with tamoxifen (180 mg/kg) intraperitoneally once per day for 5 consecutive days alternating sides as described above. Ten to 13 days after the last tamoxifen injection, mice underwent surgery for AAV2/5 *GfaABC$_1$D*-GCaMP6f microinjection in the frontal cortex, cranial window placement, and EEG & EMG electrode implantation as described above. Mice were later fitted with a baseplate 1.5 – 2.5 weeks after surgery and imaged 3 – 4 weeks later after habituation to the EEG/EMG tether and miniature microscope as described above.

On the experimental day, mice were attached to the EEG/EMG tether and miniature microscope and placed in the recording chamber. Mice were allowed at least 10 min to settle in the familiar chamber. Next, we imaged 5 mins of pre-injection astroglial Ca^{2+} activity using the miniature microscope. Mice were then injected intraperitoneally with 20 mg/kg methoxamine hydrochloride (#M6524, Sigma-Aldrich) made in saline [33]. Image capture then occurred at 0 min (t0), 20 min (t20), 60 min (t60), and 110 min (t110) post-injection for 2 min at each time point. Mice were left undisturbed during all recordings.

GSTIM1 sleep phenotyping

Male and female GSTIM1 WT (n = 8; females = 1) and GSTIM1 cKO (n = 9; females = 4) adult mice (8 – 12-weeks-old) were injected with tamoxifen (180 mg/kg) intraperitoneally once per day for 5 consecutive days alternating sides as described above. Ten days after the last tamoxifen injection, mice underwent surgery for EEG & EMG electrode implantation. Mice were allowed 5 days of recovery from surgery. Animals were then connected to a lightweight, flexible tether and allowed at least 3 days to habituate to the tether and recording environment. After habituation, mice underwent 24 h undisturbed baseline EEG & EMG recording starting at light onset (ZT0). The next day, mice were sleep deprived for 6 h via gentle handling beginning at light onset according to previously published methods [2, 63]. Mice were then allowed 18 h undisturbed recovery sleep. There were no differences between male and female mice for our sleep measures of interest with two exceptions. Female GSTIM cKO mice had fewer NREMS bouts during the BL light period (male: 9.37 ± 0.36, female: 7.79 ± 0.40; repeated-measures ANOVA, effect of sex: $F(1, 7) = 9.87$, $p = 0.016$), and there was an effect of sex on BL REMS bout duration for GSTIM cKO mice (repeated-measures ANOVA: $F(1, 7) = 9.86$, $p = 0.016$) but no significant pairwise differences.

GSTIM1 patterns in activity & core temperature

Male and female GSTIM WT (n = 3; female = 0) and GSTIM1 cKO (n = 3; female = 1) adult mice (14-weeks-old) were injected with tamoxifen (180 mg/kg) intraperitoneally once per day for 5 consecutive days alternating sides as described above. Four weeks after the last tamoxifen injection, mice were implanted with an abdominal telemetry device. Mice were allowed 8 days of recovery from surgery. Mice were then allowed 5 days to habituate to running wheels (#ENV-047, Med Associates, Inc, Fairfax, VT). After habituation, mice were recorded for 7 days under 12:12 h light:dark conditions. During this time, running wheel activity, cage activity, and core body temperature were recorded continuously.

Miniature microscope imaging with EEG & EMG

Data acquisition

Adult male mice (n = 6 C57BL/6J, n = 3 GSTIM1 WT, n = 4 GSTIM1 cKO) were connected to a counterbalanced, light-weight EEG & EMG recording tether coupled to a nano connector (#A79108-001, Omnetics, Minneapolis, MN) and a head-mountable, epifluorescent miniature microscope (nVista 2.0; Inscopix, Palo Alto, CA) coupled to a baseplate affixed to the skull. Animals were allowed at least 3 days to habituate to the recording environment. EEG & EMG data were acquired through Pinnacle Technology, Inc. Data Conditioning and Acquisition System (#8401 HS) and Sirenia Acquisition software (v1.7.7, Pinnacle Technology, Inc., Lawrence, KS). EEG data were digitized at 250 Hz, high pass filtered at 0.5 Hz, and low pass filtered at 40 Hz. EMG data were digitized at 2 kHz, high pass filtered at 10 Hz, and low pass filtered at 100 Hz. The system was set up to detect rising transistor-transistor logic (TTL) pulses generated by the imaging system, which was used to synchronize imaging frames and electrophysiological data.

Ca^{2+} imaging data was acquired through the head-mountable, epifluorescent miniature microscope and Inscopix nVista HD software (v2.0.4). Imaging frames were captured at 10.1 frames per second with an exposure time of 49.664 ms at a gain of 2.0. LED power ranged from 50 – 80% to adjust the upper tail of the histogram to be as close to a pixel value of 1500 to ensure good signal-to-noise ratio [64]. The LED power was set at the beginning of the experiment for each mouse and did not change for the remainder of the experiment. During image capture, TTL pulses were sent to the Sirenia Acquisition software at 50% duty and recorded as annotations in the EEG & EMG data file. The microscope remained in place in the baseplate for the entirety of the EEG & EMG recording period.

Data processing and analysis

Imaging data were pre-processed using the Data Processing Software (v1.2.1; Inscopix). For each animal, movies acquired during baseline and during SD and recovery were concatenated into a timeseries. This timeseries was spatially downsampled by a factor of 2 from 1440 × 1080 pixels to 720 × 540 pixels and temporally downsampled by a factor of 5 to 2 Hz to reduce the data footprint [64]. Defective pixels were also rectified [64]. Small lateral displacements were then corrected for by registering all frames to a single reference frame free of movement using the motion correction algorithm in the Data Processing Software. Next, ROIs were identified manually. Because astroglial Ca^{2+} activity is highly synchronous, the Data Processing Software PCA-ICA analysis failed to identify individual cells. Therefore, to identify individual cells, images were converted to ΔF/F images by expressing each frame as the relative change from the mean image obtained from the entire movie [$\Delta F/F_{mean} = (F - F_{mean})/F_{mean}$] [64, 65]. A spatial bandpass filter was also applied using default settings (low cut-off = 0.005; high cut-off = 0.500) to help delineate individual cells. Regions of interest (ROI) were selected by manually identifying cell-body-sized, high-contrast regions over the course of the timeseries, and contours were drawn to contain pixels from the ROI [66]. Raw fluorescent values were exported for each individual ROI for the full timeseries. ROIs were further validated by inspecting temporal traces from individual ROIs for Ca^{2+} signals consistent with Ca^{2+} transients from individual cells, and only ROIs with clearly identified signals were included in further analyses [23, 67–69]. We identified 586 individual ROIs from 6 mice. Custom MATLAB scripts were then used to align exported raw ROI fluorescent values from imaging frames with scored sleep and wake states using annotations in the EEG & EMG data generated by the TTL pulses from Inscopix nVista imaging system.

To correct for slight decays in fluorescent signal across each recording, Ca^{2+} traces for each ROI were detrended by subtracting an exponential curve fit from each individual raw Ca^{2+} imaging trace using the 'fit' function from MATLAB's Curve Fitting toolbox [70]. The exponential curve is given by:

$$y = ae^{bx}$$

where *a* is the starting fluorescent value, *b* is the decay constant, *x* is time, and *y* is the fluorescent value at time *x*. The curve fit from all recordings across the timeseries were then averaged and added back to each trace to bring traces to a common baseline. Ca^{2+} values were then expressed as percent change from the median fluorescent value of the full timeseries for each ROI:

$$\Delta F/F\ (\%) = (F_t - F_{median})/F_{median} * 100$$

where F_t is the individual detrended fluorescent value at a specific time point and F_{median} is the median fluorescent value for the timeseries [70, 71]. We used F_{median} because it is not influenced by large changes in calcium activity like other reference measurements (i.e., F_{mean}). Additionally, we computed F_{median} from all vigilance states in order to directly compare ΔF/F between vigilance states. Event detection with a 0.5% prominence threshold was then performed using the 'findpeaks' function from MATLAB's Signal Processing toolbox. Two conditions had to be met to identify an ROI's frame as an event: 1) the value of that frame is larger than its two neighboring frames, and 2) the difference between that value and the value of the larger neighboring trough (prominence) is greater than 0.5% of the range of the entire trace. Identified events were then used to determine frequency of Ca^{2+} events per 4 s epoch. Additionally, the amplitudes of these events were sorted into deciles of the range. Typically, Ca^{2+} imaging studies set a threshold (e.g., 2 standard deviations) that an event or peak must cross to be counted as an event. However, this thresholding would limit the detection of astroglial Ca^{2+} events that occur during non-rapid eye movement sleep (NREMS) and rapid eye movement sleep (REMS) because these events are smaller compared to those in wake. Instead, all detected astroglial Ca^{2+} events were binned into deciles of the range by calculating the event's amplitude as a percentage of the amplitude range of the trace across the full timeseries (i.e., across all states) rounded to the nearest 10%. To inspect Ca^{2+} signals during vigilance state transitions, Ca^{2+} data were extracted frame-by-frame for the 12 s before and after the transition. These transitions were removed from analysis for ΔF/F comparisons over time in Figure 1I and Figure S1 as more state transitions were captured during ZT6 compared to other time points. The removal of these transitions allowed for comparisons of Ca^{2+} during steady state epochs. We did not include wake-to-REMS or REMS-to-NREMS transitions as these transitions rarely occur in mice. Pearson's correlation coefficients were calculated from ΔF/F values across individual bouts of wake, NREMS, and REMS at ZT6. Vigilance state bouts used for the cross-correlation analysis were 20 – 60 s long.

Two-photon imaging with EEG & EMG

Data acquisition

During experiments, adult male mice (n = 4 C57BL/6J) were connected to a tether coupled to a nano connector. The tether was coupled to an interface box (S-Box, Tucker-Davis Technologies, Alachua, FL), transmitted EEG & EMG signals were amplified via a low impedance amp (PZ3-32, Tucker-Davis Technologies), and data were processed and recorded via the Z series 2 DSP High Performance Processor (RZ2-2, Tucker-Davis Technologies) and OpenEx software (Tucker-Davis Technologies). EEG & EMG data were digitized at 1017.3 Hz. EEG signals were high pass filtered at 0.3 Hz and low pass filtered at 30 Hz. EMG data were high pass filtered at 10 Hz and low pass filtered at 100 Hz. The system was also set up to receive and incorporate TTL pulses generated by the two-photon imaging system.

Prior to experiments, mice were habituated to increasingly prolonged periods of time in head restraint in the flat-floored, air-lifted Mobile HomeCage (Neurotar, Helsinki, Finland). During experiments, unanesthetized mice were head-fixed inside the Mobile HomeCage at least 30 min prior to imaging and then imaged using resonant scanning microscope UltimaIV running Prairie View acquisition software (Bruker Corporation, Billerica, MA). To excite, filter, collect, and detect GCaMP6f fluorescence changes in astrocyte somata and processes, we used an excitation wavelength of 920 nm (Chameleon II, Coherent Inc., Santa Clara, CA) with ET-GFP (FITC/CY2) emission filter cube (#49904, Chroma Technology Corporation, Bellows Falls, VT) with a 20x (1.0NA) XLUMPLFL20X W/IR-2 objective (Olympus, Shinjuku, Tokyo, Japan) and GaASP photo-multiplier tube (H7422-40, Hamamatsu Photonics KK, Hamamatsu City, Shizuoka, Japan). The imaged field of view was 277 × 277 μm, pixel dimensions were 0.188 × 0.188 μm, and rate of acquisition was 3.7 Hz. During frame acquisition, TTL pulses were sent from the two-photon imaging system to the Tucker-Davis Technologies system and incorporated in the EEG & EMG data file for subsequent alignment of imaging frames and electrophysiological data.

Data processing and analysis

We used ImageJ [55] and Fiji [56] for image processing. The ImageJ plugin "Kalman Filter" was applied to collected image stacks to remove high gain noise and to recover faint image details. Imaged stacks were then visually inspected frame-by-frame which occasionally revealed motion artifacts along the x- and y-axes and required registration using the "Template Matching" ImageJ plugin. Image frames along the x- and y- axes that could not be registered or any that occurred along the z axis were manually removed from analysis. These registered t stacks could then be used to produce sum projection images (sums the slices in the stack) or maximum projection images (image displaying maximum pixel values from slices in the stack) in ImageJ. For selection criteria, first, astrocyte somata and processes were identified from high resolution, maximum projected image stacks. Second, individual GCaMP6f expressing astrocytes in which the soma and its processes were captured within the same image plane and did not overlap with other cells were identified for further analysis. For signal extraction, two separate ROIs were drawn per astrocyte: one circumscribing the cell soma and one defining the territory of its processes. With the territory of the astrocyte processes delineated, a sampling-grid containing 2.7 μm x 2.7 μm squares was overlaid. Data were extracted only from those ROI grid squares contained, in their

entirety, within the circumscribed processes territory. From 4 mice, we identified n = 60 astroglial somata along with n = 6074 process ROIs.

Ca^{2+} imaging data were processed as described above for the epifluorescent imaging data for each ROI and their respective process ROIs using the custom MATLAB scripts. To compare differences in ΔF/F of the somata and processes across vigilance states, we calculated frame-by-frame difference scores by subtracting the ΔF/F value of the soma from the ΔF/F value from each associated process ROI ($\Delta F/F_{DIFF} = \Delta F/F_{Process} - \Delta F/F_{Soma}$).

We also used the Astrocyte Quantitative Analysis (AQuA) software to analyze more dynamic features of astroglial Ca^{2+} signals from two-photon microscopy data (i.e., event area, event duration, temporally co-occurring events, spatially co-occurring events) using a cross-sectional design [28]. Astrocyte soma and processes located in the same optical plane were identified via sum projections of two-photon image stacks. Two ROIs were used to delineate areas used for further analysis for each individual cell: one ROI circumventing the entire astrocyte and a second ROI circumventing the soma. We used the following recommended AQuA detection pipeline parameters to identify Ca^{2+} events [28]: *Signal*: intensity threshold scaling factor (thrARScl) = 2, smoothing_sigma (smoXY) = 1, minimum size_pixels (minSize) = 16; *Voxel*: temporal cut threshold (thrTWScl) = 2, growing z threshold (thrExtZ) = 1; *Event*: rising time uncertainty (cRise) = 2, slowest delay in propagation (cDelay) = 2, propagation smoothness (gtwSmo) = 1; *Clean*: z-score threshold (zThr) = 3; *Merge*: not used; *Recon*: temporally extend events (extendEvtRe) = not used; *Feature*: ignore decay tau (ignoreTau) = yes. Ca^{2+} events were then parsed into propagating events and static events. Propagating events were identified based on a series of algorithmic parameters to asses if a Ca^{2+} event grew, shrunk, or moved [28]. Events that did not propagate were defined as static events [28]. These propagating and static events were further parsed based on their starting distance from the soma: those that started closer to the soma (i.e., < 50%) and those that started farther from the soma (i.e., > 50%) based on the distance between the soma and the cell border [28]. We determined the area (i.e., size in μm^2) and duration (i.e., length of event onset to event offset in seconds) of each propagating and static astroglial Ca^{2+} event [28]. We also used a separate set of AQuA algorithms to identify the number of Ca^{2+} events that either overlapped in time (i.e., temporally co-occurring events) or overlapped in space (i.e., spatially co-occurring events) [28]. Temporally and spatially co-occurring events were determined within individual astrocytes and included all events within the cell irrespective of the event's location (e.g., soma, processes) [28].

Sleep phenotyping

EEG & EMG data were collected with a Grass 7 polygraph system (Natus Medical Incorporated, Pleasanton, CA) via a light-weight cable for sleep phenotyping experiments in GSTIM1 WT and cKO mice. EEG & EMG signals were amplified and digitized at 256 Hz using VitalRecorder acquisition software (SleepSign for Animal, Kissei Comtec Co., LTD, Nagano, Japan). EEG & EMG data were high- and low-pass filtered at 0.3 and 100 Hz and 10 and 100 Hz, respectively.

All EEG & EMG data (including data collected with the Pinnacle Technology, Inc. and Tucker-Davis Technologies systems) were scored using SleepSign for Animal. Wake, NREMS, and REMS were determined by visual inspection of the EEG waveform, EMG activity, and fast Fourier transform (FFT) analysis by an experimenter blinded to experimental conditions. Data were scored as wake, NREMS, or REMS with 4 s resolution as previously described [2, 60]. Bout lengths were defined as ≥ 7 consecutive epochs (≥28 s) for wake and NREMS and ≥ 4 consecutive epochs (≥16 s) for REMS.

The EEG was subjected to FFT analysis to produce power spectra between 0 – 30 Hz with 0.5 Hz resolution. Delta (δ) was defined as 0.5 – 4 Hz and low delta as 0 – 1.5 Hz [2]. For genotypic comparisons of EEG spectral data, each spectral bin was expressed as a percentage of the total power in baseline wake, NREMS, and REMS averaged across the 3 states. For hourly NREM delta power (i.e., NREM slow wave activity) analysis after SD, spectral values within the delta band or low delta band for each hour were normalized to the average NREM delta or low delta band value, respectively, from the last 4 h of the baseline light period (ZT8 – 11) and expressed as a percentage [22]. EEG epochs containing visually-detected artifacts were excluded from spectral analyses. Two GSTIM1 cKO mice were removed from spectral analyses due to artifact.

QUANTIFICATION AND STATISTICAL ANALYSIS

Plots were generated in SigmaPlot (v11.0, Systat Software, Inc., San Jose, CA) and R (v3.6.0) [57]. For simplicity, outliers were not plotted with boxplots. Actograms of wheel running activity and heatmaps of cage activity and core body temperature were made in Microsoft Excel [72]. Statistical analyses were performed using SPSS for Windows (IBM Corporation, Armonk, NY) unless otherwise noted. Statistical details are provided in the main text and figure legends. Data are presented as means ± standard error of the mean (SEM) unless otherwise stated. Normality of the data was determined with Shapiro-Wilk or Kolmogorov-Smirnov tests. Comparisons of baseline ΔF/F, events per epoch, amplitude deciles, Pearson correlation coefficients, and process-somata difference scores across vigilance states were made using Friedman tests. *Post hoc* pairwise comparisons were made using Wilcoxon signed rank tests with Bonferroni corrections. The mice, mitml, and lme4 R packages were used to compare NREMS ΔF/F values and NREM EEG delta power across ZT0, 6, and 12 with multiple imputations using the 2l.pan mixed-effects model and 100 imputations. The imputed models were then fit using a linear mixed-effects model through the lmer function with individual mice as a random effect. *Post hoc* pairwise comparisons of the fitted model were made with the emmeans function and Tukey correction. Comparisons of events/epoch and ΔF/F values between somata and processes were made with the Mann-Whitney U test. Comparisons of ΔF/F values between baseline and SD days were made with Wilcoxon signed rank tests. Comparisons of area, duration, temporally co-occurring events, and spatially co-occurring events between vigilance states were made with the Wilcoxon signed rank test.

Comparisons of area, duration, temporally co-occurring events, and spatially co-occurring events between baseline and SD days were made with Mann-Whitney U tests. Comparisons of the cumulative probability curves for area and duration between subcellular region (i.e., < 50% versus > 50%) were made with Kolmogorov–Smirnov tests. For static events, these comparisons were restricted to values that fell below the saturation point. We defined the saturation point as the area or duration that corresponded to a cumulative probability value $\geq$ 0.99. Based on this criterion, the area saturation point was set at 8 μm^2 and the duration saturation point was set at 14 s. Correlations made between area or duration versus starting proximity to the soma for propagating and static Ca^{2+} events were made using Pearson's correlation tests. Comparisons of these correlations based on treatment (BL versus SD) were made using Fisher's Z-transformation tests. Comparisons of $\Delta F/F$ values between GSTIM1 WT and GSTIM1 cKO mice at baseline, after SD, and post-methoxamine treatment were made using Mann-Whitney U tests. For sleep phenotyping and analysis of diurnal/nocturnal temperature and activity patterns, a general linear model for repeated-measures (RM) using time (hours or period) as the repeated-measure and genotype (GSTIM1 WT versus GSTIM1 cKO) as the between subjects factor was used when multiple measurements were made over time (i.e., time-in-state, bout number, bout duration, hourly NREM delta power, running wheel activity, cage activity, core body temperature). Repeated-measures were tested for sphericity, and a Greenhouse-Geisser correction was applied when appropriate. *Post hoc* pairwise comparisons using Sidak corrections were performed when there were significant interaction effects or main effects of genotype. Baseline time-in-state and bout data RM comparisons were made over all time intervals during the full 24-h recording period (ZT0 - 23). Running wheel activity, cage activity, and core body temperature RM comparisons were made over all time intervals for the full 7-d recording period. For SD experiments, RM comparisons were made over all time intervals during the full recovery period (ZT6 – 23) for time-in-state data. Comparisons of 2 h averages of NREM delta power post-SD were made with RM over ZT6 – 11 of the recovery phase. Comparisons of normalized EEG spectral power during baseline and after SD were made using RM comparison from 0 – 30 Hz with spectral power as the dependent variable and genotype as the between-subjects factor. If the RM comparisons yielded a significant result, unpaired Student's t tests with Benjamini-Hochberg correction were then used for comparisons of individual EEG spectral frequency bins with genotype as the grouping variable. Unpaired Student's t tests with genotype as the grouping variable were used to analyze total sleep time post-SD. An alpha level of 0.05 was used to indicate significance.